Science of the Total Environment 862 (2023) 160694

Contents lists available at ScienceDirect

Science of the Total Environment

journal homepage: www.elsevier.com/locate/scitotenv

Hydrogeochemical and isotopic characterization of the Gioia Tauro coastal Plain (Calabria - southern Italy): A multidisciplinary approach for a focused management of vulnerable strategic systems

G. Vespasiano [a,b], G. Cianflone [a,b,*], L. Marini [c], R. De Rosa [a], M. Polemio [d], K. Walraevens [e], O. Vaselli [f,g], L. Pizzino [h], D. Cinti [h], F. Capecchiacci [f,g,i], D. Barca [a], R. Dominici [a,b], C. Apollaro [a]

[a] Department of Biology, Ecology and Earth Sciences (DIBEST), University of Calabria, Via Ponte Bucci 4, Cubo 15B, 87036 Rende, Italy
[b] E3 (Earth, Environment, Engineering) Soc. Coop. and Spin-Off of University of Calabria, Via Ponte Bucci, Cubo 15B, 87036 Rende, Italy
[c] Steam Srl, Via Ponte a Piglieri 8, I-56121 Pisa, Italy
[d] CNR-IRPI, National Research Council, Research Institute for Hydrogeological Protection, Via Amendola 122 I, 70126 Bari, Italy
[e] Laboratory for Applied Geology and Hydrogeology, Department of Geology, Ghent University, 9000 Ghent, Belgium
[f] Department of Earth Sciences, University of Florence, Via G. La Pira 4, 50121 Firenze, Italy
[g] CNR-IGG Institute of Geosciences and Earth Resources, Via G. La Pira 4, 50121 Firenze, Italy
[h] Istituto Nazionale di Geofisica e Vulcanologia, Sezione di Roma 1, Via di Vigna Murata 605, 00143 Rome, Italy
[i] Istituto Nazionale di Geofisica e Vulcanologia, Sezione di Napoli, Osservatorio Vesuviano, Via Diocleziano, 328, 80125 Napoli, NA

HIGHLIGHTS

- Marine intrusion is very localized despite the high groundwater demand.
- In the deep aquifer, Na-Cl connate waters with high Cl and B concentrations.
- Na-Cl water with higher temperature along a main fault.
- In deep aquifer, Na-HCO_3 waters due to water-rock interaction with crystalline rocks.
- Anthropic sources of N and SOx affect the shallow aquifer.

GRAPHICAL ABSTRACT

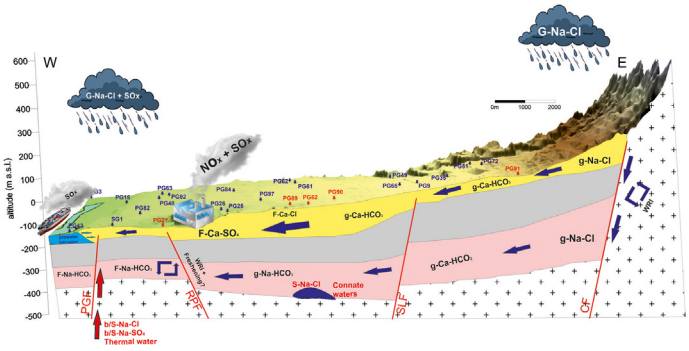

ARTICLE INFO

Editor: José Virgílio Cruz

Keywords:
Coastal aquifers
Hydrogeochemistry
Water isotopes
Conceptual hydrogeochemical model
Calabria
Southern Italy

ABSTRACT

This work pursues the hydro-geochemical and isotopic characterization of the complex groundwater system of the Gioia Tauro Plain, one of the most important industrialized and agricultural coastal areas of southern Italy. The anthropic pressure exposes the water resources at risk of depletion and quality degradation making the plain groundwater a system of high scientific and social interest.

The plain is characterized by a shallow aquifer, mostly recharged by local rains and a deep aquifer apparently less influenced by local precipitation. Both aquifers are mainly Ca-HCO_3 waters except for localized sectors where Na-HCO_3, Na-Cl and Ca-SO_4 waters are present. In deep aquifer, both prolonged interaction with sedimentary rocks, mainly deriving from the erosion of crystalline rocks, and direct cation exchange represent the primary factors controlling the formation of Na-HCO_3 waters. Mixing processes between these waters and either connate brine and/or deep thermal waters contribute to the formation of isolated high salinity Na-Cl-rich waters. In shallow aquifer, inputs of N-rich sewage and agriculture-related contaminants, and SOx emissions in proximity of the harbor are responsible of the

* Corresponding author at: Department of Biology, Ecology and Earth Sciences (DIBEST), University of Calabria, Via Ponte Bucci 4, Cubo 15B, 87036 Rende, Italy.
E-mail address: giuseppe.cianflone@unical.it (G. Cianflone).

http://dx.doi.org/10.1016/j.scitotenv.2022.160694
Received 16 September 2022; Received in revised form 14 November 2022; Accepted 1 December 2022
Available online 6 December 2022

increasing nitrate and sulphate concentrations, respectively. The Cl/Br and NO_3/Cl ratios highlight contamination mainly linked to agricultural activities and contribution of wastewater.
Along the northern boundary, the warmest groundwater (Na-Cl[SO_4]) were found close to a bend of the main strike-slip fault system, locally favouring the rising of B- and Li-rich deep waters, testifying the influence of geological-structural features on deep water circulation.
Despite the high-water demand, a direct marine intrusion is localized in a very restricted area, where we observed an incipient groundwater-seawater mixing (seawater contribution ≤7 %). The qualitative and quantitative conditions of the shallow aquifer still have acceptable levels because of the relatively high recharge inflow. A reliable hydrogeochemical conceptual model, able to explain the compositional variability of the studied waters, is proposed.

1. Introduction

During the last years, the sustainable management of coastal plains have received significant attention worldwide (e.g., Boughriba and Jilali, 2018; Matiatos et al., 2018; Vespasiano et al., 2015a, 2019; Mastrocicco and Colombani, 2020; Polemio and Zuffianò, 2020; Cianflone et al., 2021; Sarker et al., 2021; Nisi et al., 2022). Coastal plains show an important economic, social, and biological value as they represent the link between marine and terrestrial environments (Martínez et al., 2007). In response to this, coastal plains have always been considered strategic sectors for human settlement hosting most of the world's megacities with the relative issues due to the intensive use of the territory (McGranahan et al., 2007). In these areas, the intensive exploitation of groundwater reduces freshwater outflow to the sea, forming a local water table depression and inland seawater migration (Masciopinto, 2006; Mjemah et al., 2009; Van Camp et al., 2014). This phenomenon, named seawater intrusion, is a global concern and represents one of the most widespread processes that degrade groundwater quality and limit its utilization (Nisi et al., 2013; Alfarrah and Walraevens, 2018; Vespasiano et al., 2019; Boumaiza et al., 2020; Han et al., 2021; Kammoun et al., 2021). Coupled with a continuing sea level rise due to global warming, coastal aquifers are expected to be threatened in a relatively near future (Alfarrah and Walraevens, 2018). Consequently, there has been an increasing interest in evaluating the extent of seawater intrusion in response to overexploitation and sea level rise (Barlow and Reichard, 2010; Custodio, 2010; Polemio and Walraevens, 2019). Seawater intrusion phenomena have been reported in many coastal areas of the United States of America (Barlow, 2003; Langman and Ellis, 2010), Africa (El Halimi et al., 2001; Steyl and Dennis, 2010; Van Camp et al., 2013; Walraevens et al., 2015; Alfarrah and Walraevens, 2018) and, to a lesser extent, of Mexico (Cardoso, 1993), South America (Bocanegra et al., 2010), Saudi Arabia (Alshehri et al., 2021) and Australia (Werner, 2010). Also in Italy, studies focused on the sustainable management and characterization of the main processes linked to marine intrusion have undergone a considerable increase (e.g., Capaccioni et al., 2005). From the northern-central to the southernmost coasts of the Adriatic and Tyrrhenian Seas, as well as in Sardinia and Sicily, several areas were recognized to be at risk of salinization (e.g., Barrocu, 2003; Grassi et al., 2007; Brozzo et al., 2011; Mollema et al., 2013; Felisa et al., 2013; Iyalomhe et al., 2015; Franceschini and Signorini, 2016; Vespasiano et al., 2016; Vespasiano et al., 2019; Muzzillo et al., 2021; Bellafiore et al., 2021; Giambastiani et al., 2021; Mastrocicco et al., 2021; Cianflone et al., 2021, 2022), similarly to what is occurring in other coastal areas of the Mediterranean Sea (e.g., Alcalá and Custodio, 2008; De Montety et al., 2008; Custodio, 2010; Mastrocicco and Colombani, 2020).

Complex geological setting, mixing between marine and connate waters, ion exchange processes and natural and/or human-induced inputs (due to industrial and agricultural activities) represent other conditions that can modify groundwater composition of coastal plains (Mollema et al., 2013; Mtoni et al., 2013; Carreira et al., 2014; Corniello et al., 2015; Abu Al Naeem et al., 2019; Vespasiano et al., 2019; Mastrocicco et al., 2021). In these contexts, sources and driving mechanisms are to be identified and characterized by a multidisciplinary approach (including geological, hydrogeological, geochemical, and geophysical investigations), to produce reliable conceptual and numerical models whose results can be used for steering suitable preventive actions. Water geochemistry and isotopes (e.g., $^{18}O/^{16}O$ and $^{2}H/^{1}H$ ratios) are useful to: i) identify the main ongoing water-rock interaction processes, leading to the formation of the different geochemical facies (Vespasiano et al., 2019); ii) evaluate freshwater-saltwater interactions as well as consequent ion exchange and oxidation–reduction reactions (e.g., Zarei et al., 2012; Sudaryanto and Naily, 2018); iii) contribute to the management of the groundwater resource (e.g., Menichini and Doveri, 2020; Carrión-Mero et al., 2021); iv) model transport pathways and fate of saline water (e.g., Ganyaglo et al., 2017; Wua et al., 2020); v) evaluate the environmental impact induced by human activities, if any, and vi) assess groundwater quality (e.g., Apollaro et al., 2019a, 2019b; Vardè et al., 2019; Apollaro et al., 2020; Figoli et al., 2020; Alshehri et al., 2021; Mastrocicco et al., 2021; Apollaro et al., 2022). In coastal plains, a detailed geochemical characterization of the aforementioned processes represents the primary objective to promote sustainable management and intervene purposefully for the resolution and/or mitigation of possible problems (Fehdi et al., 2009; Bompoti et al., 2015; Mallick et al., 2018).

This work is aimed at investigating the Gioia Tauro Plain (GTP) groundwater system. GTP is located along the south-western coast of the Calabria Region and is one of the most important industrialized and coastal agricultural areas of southern Italy, with an extension of about 500 km^2. The plain is inhabited by about 160,000 people distributed in towns, villages, and rural areas. It is characterized by a highly developed agricultural sector and two thermoelectric industries (waste-to-energy and thermoelectric power plants). Furthermore, GTP hosts two strategic infrastructures such as the Gioia Tauro Harbor (the largest transhipment terminal of Italy and one of the most important container traffic hubs in the Mediterranean basin) and the A2 “Mediterranea” highway (the main road line of the Region).

Despite the crucial role and the presence of relevant infrastructures, GTP still presents portions completely devoid of basic services, such as sewers or connections to aqueducts for domestic use. The lack of such services and the well-developed anthropic activities expose the GTP groundwater resources at risk of depletion and quality degradation. Furthermore, GTP shows a very articulated geological and structural framework that locally favour the development of waters with chemical characteristics not fully explainable by typical water-rock interaction processes occurring in the sedimentary aquifers and/or seawater intrusion (Pizzino et al., 2004; Cianflone et al., 2021). In addition to the ongoing anthropic pressure (mainly due to intensive farming), this issue makes the GTP groundwater a system of high scientific and social interest.

This work has as main target that to improve the hydrogeological and geochemical knowledge of the GTP groundwater systems by providing new geochemical and isotopic data to i) assess the main processes affecting the main GTP aquifers and ii) establish the relationship between natural and anthropogenic sources that concur to the observed water chemistry variability and iii) propose a conceptual model of fluid circulation.

2. Geological, structural, and hydrogeological settings

GTP is a NNE-SSW oriented half-graben (Fig. 1a) of Upper Pliocene-Pleistocene age (Monaco and Tortorici, 2000), bounded to the east by the NNE-SSW Cittanova Fault (CF_NNE-SSW_W) [*fault acronym_strike_dip*]

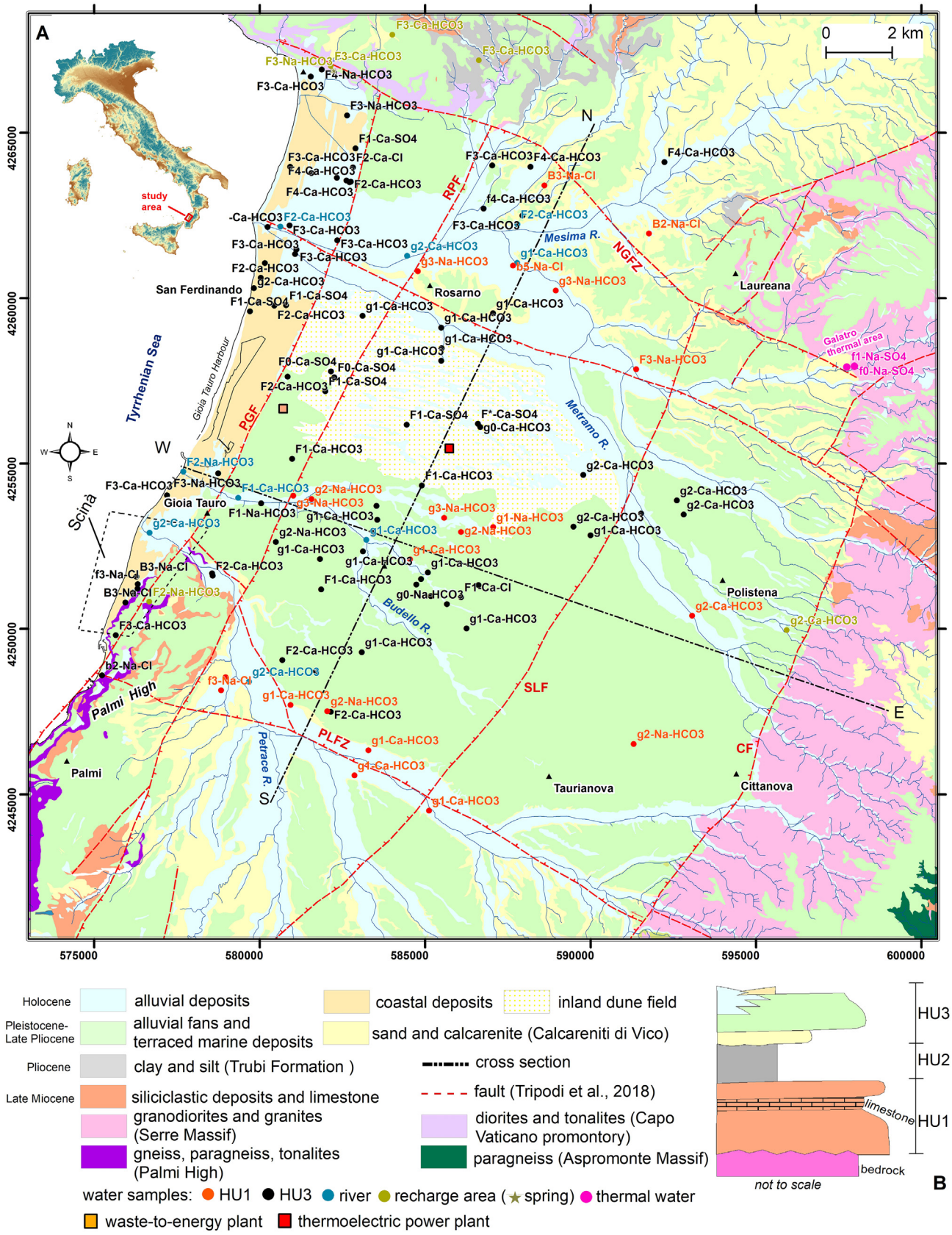

Fig. 1. (a) Simplified geological map of the Gioia Tauro area (modified after Cianflone et al., 2021) showing location and ID (Stuyfzand, 1986) of water samples (red symbols: deep aquifer; black symbols: shallow aquifer); (b) schematic stratigraphic column (not to scale) showing the deep (HU1) and shallow (HU3) aquifers and the aquitard (HU2) recognized in the study area. NGFZ: Nicotera-Gioiosa Fault Zone; PGF: Palmi-Gioia Tauro Fault; RPF: Rosarno-Palmi Fault; SLF: Sant'Eufemia-Laureana Fault; CF: Cittanova Fault; PLFZ: Palmi-Locri Fault Zone.

(Figs. 1a and 1Sa), a high-angle, west-dipping, master normal fault and juxtaposing the crystalline bedrock and the GTP sedimentary infill (Jacques et al., 2001; Tripodi et al., 2018). CF was responsible for both the 1783 catastrophic earthquake (Mw = 7.0) and the seismic event that occurred in the 4th century CE (Galli and Peronace, 2015; Galli and Bosi, 2002). Other three faults parallel to CF occur in the study area: the west dipping Sant'Eufemia-Laureana Fault (SLF_NNE-SSW_W) and the Palmi-Gioia Tauro Fault (PGF_NNE-SSW_W) and an east dipping tectonic structure occupying an intermediate position between SLF and PGF: the Rosarno-Palmi Fault (RPF_NNE-SSW_E) (Tripodi et al., 2018). Furthermore, two other faults, orthogonal to CF, occur: (i) to the North, the Nicotera-Gioiosa Fault Zone (NGFZ_NW-SE_S), NW-SE striking and with right strike-slip kinematics, (ii) to the South, the Palmi-Locri Fault Zone (PLFZ_NW-SE_N), of NW-SE direction and a main left strike-slip kinematics (Tripodi et al., 2018 and references therein). According to Loreto et al. (2019), the GTP depression represents the emerged portion of the Gioia Tauro Basin, extending offshore in the Tyrrhenian Sea, while NGFZ is the subaerial part of an important tectonic structure continuing for some tens of km in the Tyrrhenian Sea and delimiting to the south the Capo Vaticano Ridge.

The eastern and northern sides of the plain are bounded by the Serre Massif, a complete continental crustal section made up of Variscan metamorphic and plutonic rocks (Cirrincione et al., 2015). The Serre Batholith crops out along the eastern boundary and includes two-mica porphyritic granodiorites and granites, two-mica granodiorites and granites, and biotite granodiorites (Fig. 1a). The Capo Vaticano Promontory is a sector of the Serre Massif separated from the main body by the Mesima graben. It bounds the NW-sector of the plain and is made up of qz-diorites and tonalites, and a migmatitic border zone. To the south of Cittanova town, PLFZ_NW-SE_N separates the Serre Massif from the Aspromonte Massif (Cirrincione et al., 2015). In this sector, the latter consists of migmatitic paragneisses, which outcrop in the catchment of the Petrace River. The GTP southwestern side is bounded by the Palmi High, characterized by crystalline rocks (migmatitic paragneiss, foliated tonalite and augen gneiss) covered by Tortonian-Messinian siliciclastic and carbonate deposits (Cirrincione et al., 2015).

The GTP basin is filled by a sedimentary succession starting with upper Miocene siliciclastic and carbonate deposits, which unconformably cover the crystalline bedrock (Fig. 1a). The succession passes upward to thick (~600 m) Plio-Pleistocene marine sediments (Jacques et al., 2001), which include, at their bottom, Pliocene clayey and silty deposits, hundred meters thick (Jacques et al., 2001), called “Trubi Formation” (ISPRA, 2016), and characterized in the upper part by the presence of a pumice-rich horizon (De Rosa et al., 2008). The Trubi Formation is covered, through a slight angular unconformity, by the Late Pliocene-Pleistocene Calcareniti di Vinco, consisting of cross-bedded sands and calcarenites (Jacques et al., 2001; ISPRA, 2016), which are considered as the infilling of the Siderno paleo-strait (Longhitano et al., 2012). The Late Pleistocene gravel and sand alluvial fan deposits of the Taurianova Synthem cover the Calcareniti di Vinco through an erosive contact, in the eastern side of the plain (ISPRA, 2016). The sedimentary infill of the GTP is closed by Late Pleistocene–Holocene sand- to gravel-terraced marine deposits (up to 20 m thick) and Holocene terrains where ancient aeolian inland dunes, recent alluvial deposits (in the eastern and middle sectors), and coastal deposits (in the western sector) were recognized.

From a hydrogeological point of view, the GTP sub-surface hosts (i) a deep aquifer hosted in the Late Miocene succession (HU1) and characterized by artesian condition, (ii) an aquitard (HU2) made up of Pliocene clayey and silty deposits and (iii) a shallow phreatic aquifer corresponding to the Late Pleistocene and Holocene marine and alluvial sediments, with hydraulic conductivity ranging from 10^{-4} to 10^{-5} m/s, somewhere with peaks of 10^{-3} m/s (HU3) (Fig. 1b). A peculiar hydrogeological setting characterizes the Scinà area (Fig. 1a) where the shallow aquifer (HU3), consisting of fluvial and deltaic sediments of the Petrace River and coastal deposits, lies directly over the metamorphic basement (Cianflone et al., 2021). The occurrence of deeper water circuits within the crystalline basement is indicated by both the Galatro thermal springs (Apollaro et al., 2019a, 2019b; Randazzo et al., 2022), in the north-eastern border of the study area (Fig. 1a), and B- and Li-rich waters along the NGFZ_NW-SE_S (Pizzino et al., 2004). The groundwater flow in the shallow aquifer (Fig. 2Sa) has a prevalent SE-NW direction.

The GTP comprises four main catchments (Fig. 2Sb): (i) the Mesima basin (extension of about 815 km^2), in the northern sector with a SW, W and, subordinately, NW drainage. The basin drains the Serre Massif and, partially, the Aspromonte Massif with the tributary Metramo River; (ii) the Budello basin, in the central portion, showing a W-NW drainage, a small catchment and a torrential watercourse; (iii) the Petrace basin, located in the southern sector, showing a N and NW drainage direction from the Aspromonte Massif (extension of about 420 km^2) and iv) the small (about 20 km^2) San Giovanni basin, in the northernmost side of the plain with a main NS flow direction draining the Capo Vaticano promontory.

The mean annual rainfall distribution was analyzed according to Cianflone et al. (2015). Data from 26 rain gauges (Regione Calabria – ARPACAL - https://www.cfd.calabria.it) were used to define the correlation between the Average Annual Rainfall (AAR) and Altitude (ALT) ($AAR = 1.0409 \times ALT + 846.08$, $R^2 = 0.7$). Then, we converted a DTM 20 × 20 m (Geoportale Nazionale, n.d.) from raster to a point shapefile (one point for each cell) with associated altitude data. For each point, the previously obtained correlation was applied. Finally, the punctual data were processed using the ordinary kriging as interpolation technique to obtain a continuous spatial reconstruction of the average annual rainfall (Fig. 2Sb), which is characterized by a mean annual value of 1274 mm.

3. Methods

3.1. Sampling and analytical methods

The hydrogeochemical survey at GTP was carried out from March to October 2021. A total of 114 water points, including wells, rivers, and springs were selected for water level measurement, physicochemical field measurements and geochemical (major and trace solutes) and isotopic ($\delta^{18}O$ and $\delta^{2}H$) laboratory analyses (Table 1S). The water samples were identified with a progressive number preceded by a prefix: PG: well; FG: river and SG: spring (Fig. 1Sa). The well groundwater samples were collected during pumping and the water level measurements were performed beforehand pumping (for the elaboration of groundwater levels see Cianflone et al., 2021). Wells were previously purged with international standard criteria (generally low flow and pumping of 3–4 volumes of well water column); and the samples were collected once the physicochemical parameters stabilized. The 114 samples included: 78 samples of the shallow aquifer (using wells from 5 to 100 m depth), 21 samples from the deep confined aquifer (using artesian wells from 90 to 436 m depth), 9 samples from rivers (FG1, FG2, and FG3 of Budello River; FG4, FG5, and FG6 of Mesima River; FG7 of Metramo River; FG8 and FG9 Petrace River). Furthermore, 6 samples (5 from wells drilled in the metamorphic-crystalline basement and 1 from a spring), representative of the main recharge areas, were collected: Palmi High (PG94), Aspromonte massif (PG36) and Capo Vaticano High (PG16, PG17, SG4 and PG71) (Fig. 1Sa). The three recharge areas were treated separately, given the compositional differences of the outcropping lithotypes that could affect the composition of the recharge waters.

The assignment of each well to the shallow (HU3) or deep aquifer (HU1) was carried out by comparing the well depth with the reconstructed stratigraphy, considering artesian or phreatic evidence.

It was generally assumed that groundwater samples are mainly representative of the deepest part of wells, if they were bored to tap groundwater and not for monitoring purposes (boring local companies usually are paid to drill up to find enough groundwater).

Intrinsically unstable parameters (total alkalinity, temperature, pH, and Eh) and electrical conductivity (EC) were measured in the field by means of portable instruments (Hanna instruments - *HI9829*). Two pH buffers, with nominal pH values of 4.01 and 7.01 at 25 °C, were used for pH calibration at each sampling site. The ZoBell's solution (Nordstrom, 1997) was utilized

to calibrate the mV-meter for Eh measurement. Total alkalinity was determined by acidimetric titration, using HCl 0.05 N as titrating agent and methyl-orange as indicator (Nisi et al., 2019; Vaselli et al., 2021). All water samples were filtered in situ through a membrane with a 0.45 μm pore size (e.g., Kennedy et al., 1974; Laxen and Chandler, 1982). Water samples for the determination of anions were stored without additional treatments, whereas samples for the determination of cations, trace (B, Li, Al, Fe and Mn) elements, and SiO_2 were acidified by adding suprapur acid (1 % HNO_3). All the samples were stored in polyethylene bottles, previously washed with dilute HNO_3 and rinsed with Milli-Q demineralized water. Blank solutions were prepared in the field using demineralized water and following the same procedure. All the water samples were kept at 4 °C and dark conditions before analysis. To measure the δ^2H and $\delta^{18}O$ values, 0.05 L of water was transferred into tightly sealed screw-cap bottles without filtering. Waterproof tape was bound around the cap to ensure that no evaporation took place.

The main solutes were determined by High Performance Liquid Chromatography (HPLC) by using a Thermo Scientific Dionex™ ICS-1100 equipped with Dionex IOnPac AS23 and Dionex IonPac CS12A columns for the determination of anionic (F^-, Cl^-, Br^-, SO_4^{2-} and NO_3^-) and cation (K^+, Na^+, Li^+, Ca^{2+}, NH_4^+ and Mg^{2+}) species, respectively, whereas, trace elements (B, Al, Fe and Mn) were determined with a quadrupole inductively coupled plasma-mass spectrometer which utilizes a dynamic reaction cell for interference removal (ICP-MS, PerkinElmer/SCIEX, ELAN DRC-e). On the same day of collection, dissolved reactive SiO_2 was measured by VIS spectrophotometry upon reaction with ammonium molybdate in acid media (and treatment with oxalic acid) to form a yellow silicomolybdate complex, whose absorbance was read at 410 nm (see Nollet and De Gelder, 2007 for further details). Data quality for major components was evaluated by calculating the electroneutrality parameter (EP; Appelo and Postma, 2005) or charge balance, as follows:

$$EP = [(\Sigma cat - \Sigma an)/(\Sigma cat + \Sigma an)]*100$$

The sum of cations (Σcat) and anions (Σan) are in meq L^{-1}. The EP was always less than ±5 %. Precision and accuracy for minor and trace elements was checked against the NIST1643f standard reference solution. Deviations from the certified concentrations resulted to be lower than 5 %. The δ^2H and $\delta^{18}O$ (both in ‰ vs. V-SMOW) values were measured in the Laboratories of the Stable Isotopes at the University of Florence by a Picarro L2130-i isotope analyzer, which utilise a cavity ring-down spectroscopy (CRDS) technology. The internal standards are originally inter-calibrated by using the IAEA international standards. During the instrumental setup, the possible "salinity" effects were verified. In particular, at MilliQ water increasing amounts of suprapur (dried) NaCl were added up to salinity similar or even higher than that of seawater were achieved. During these tests no significant differences were recorded. The vaporization system indeed uses a protective septum to reduce the deposition of salt in the vaporization chamber. Additionally, when dealing with saline samples we test the accuracy of our instrument with an internal seawater from the Mediterranean Sea that has been cross-analyzed with other isotopic labs, e.g. the INGV Vesuvian Observatory. It is also to mention that Picarro L2130-i has 7 positions for each line, in each line one position is dedicated to MilliQ water to control any drifts. Before each run, the internal standards are analyzed 3 to 4 times and then, every 12 samples and at the end of the any analytical session to verify and optimize the calibration. Each sample is analyzed seven times and the first 3 measurements are excluded from the post-process program to avoid any memory effects. Measurement precision, based on the repeated analysis of in-house standards, was found to be ±0.67 ‰ for δ^2H and ± 0.09 ‰ for $\delta^{18}O$. In terms of accuracy, the error is ±0.34 ‰ for δ^2H and ± 0.055 ‰ for $\delta^{18}O$.

3.2. Data processing

The final aim of the data interpretation is to elaborate a site-specific conceptual model of GTP based on geochemical/isotopic data as well as on geological and hydrogeological evidence. Thus, the study area was divided in 6 main sectors (Fig. 1Sb), as a function of the lithological-structural framework: Sector A (eastern portion-recharge area), B (northern portion across the NGFZ_NW-SE_S), C (north-central portion), D (south-central portion), E (Scinà Area) and F (southern portion across the PLFZ_NW-SE_N).

The geochemical data collected during this work were also compared with those of the Galatro thermal waters (Pizzino et al., 2004; Apollaro et al., 2019a, 2019b) since the latter likely represent the discharge at surface of the main deep thermal system present in the study area.

The geochemical data were interpreted according to consolidated procedures, such as: (i) the Durov diagram (Durov, 1948 – Fig. 2); (ii) the Total Ionic Salinity (TIS) diagram of ($Ca^{2+} + Mg^{2+}$) vs. ($Na^+ + K^+$) (Fig. 3a and b), in which the isoTIS lines are drawn for reference (Apollaro et al., 2019a, 2019b; Vespasiano et al., 2021a; Vespasiano et al., 2021b); (iii) binary plots between mobile and conservative components. Saturation indexes (SI) were calculated for selected mineral phases using the PHREEQC interactive software, *version 3.1.1* (Parkhurst and Appelo, 1999) and the LLNL thermodynamic database (Table 1S).

In the Durov diagram, the result is a representation of nine fields (from $^{(a)}$ to $^{(i)}$ in Fig. 2) that allows to separate properly the four main chemical facies generally recognized in coastal areas [Na-$HCO_3^{(c)}$, Na–$Cl^{(i)}$, Ca–$HCO_3^{(a)}$ and Ca–$Cl^{(g)}$] as well as the mixed chemical types occupying intermediate positions (Petalas et al., 2009).

A complete description of the GTP waters was performed according to their chemical and physical features by adopting a simplified version of the classification approach proposed by Stuyfzand (1989). Water classification by Stuyfzand (1989) is commonly applied to ground and surface waters occurring in coastal areas and used to identify cation exchange reactions and specific geochemical processes, which possibly control their water chemistry (e.g., Giménez-Forcada et al., 2010; Marconi et al., 2011; Vandenbohede and Lebbe, 2012; Mendizabal et al., 2012; Mollema et al., 2013; Sarker et al., 2021; Alfarrah and Walraevens, 2018).

The approach of Stuyfzand (1989) implies the step-by-step determination of the main type, type, subtype, and class (Base Exchange Index - BEX) of each water sample. Each of these four levels of classification is recorded in the total code (and name) of the water type. The main type of water is based on Cl^- concentration (in mg/L). These are G = very oligohaline: <5; g = oligohaline: 5–30; F = fresh: 30–150; f = fresh-brackish: 150–300; B = brackish: 300–1000; b = brackish-salt: 1000–10,000; S = salt: 10,000–20,000 and H = hyperhaline: >20,000 (Table 1S).

Alkalinity (in meq L^{-1}) determines the type and may vary from very low (<0.5 meq L^{-1}) to extremely high (>256 meq L^{-1}). The type includes a total of 10 "classes" of values coded from * to 9 (see Table 2S). In most natural waters with 4.5 ≤ pH ≤ 9.5 (at 25 °C, 1 bar), alkalinity is equal to the sum of HCO_3^- and CO_3^{2-} (Stuyfzand, 1989) or only HCO_3^- ion for pH ≤ 8.3 (at 25 °C, 1 bar), as is the case for the GTP waters. Nevertheless, it must be kept in mind that alkalinity is defined as the sum of all the bases dissolved in the aqueous solution and, therefore, it receives the contributions of several other dissolved anions (e.g., phosphate anions, namely PO_4^{3-} and HPO_4^{2-} entirely and $H_2PO_4^-$ in part, OH^-, $H_3SiO_4^-$, $H_2BO_3^-$, HS^-, CH_3COO^- and other organic acid anions) and neutral species (e.g., NH_3), which may become even more important than HCO_3^- and CO_3^{2-} for high-pH Ca(Mg)-OH waters (e.g., Bruni et al., 2002; Cipolli et al., 2004), formation waters (Palandri and Reed, 2001), and geothermal brines affected by boiling (Cioni and Marini, 2020).

The identification of subtypes is based on the dominant cations and anions, by using the triangular diagrams of ($Ca^{2+} + Mg^{2+}$) – ($Na^+ + K^+ + NH_4^+$) – ($Al^{3+} + H^+ + Fe^{2+} + Mn^{2+}$) and ($HCO_3^- + CO_3^{2-}$) – ($Cl^-$) – ($SO_4^{2-} + NO_3^- + NO_2^-$) both prepared adopting the concentrations in meq L^{-1}.

Finally, BEX defines the *class* and identifies the cation exchange reactions occurring during the infiltration of either saline water in a freshwater aquifer or freshwater into a saline/brackish aquifer containing several exchangers (e.g., including clay minerals, organic matter, and metal oxyhydroxides), as typically found in coastal areas. Indeed, during marine

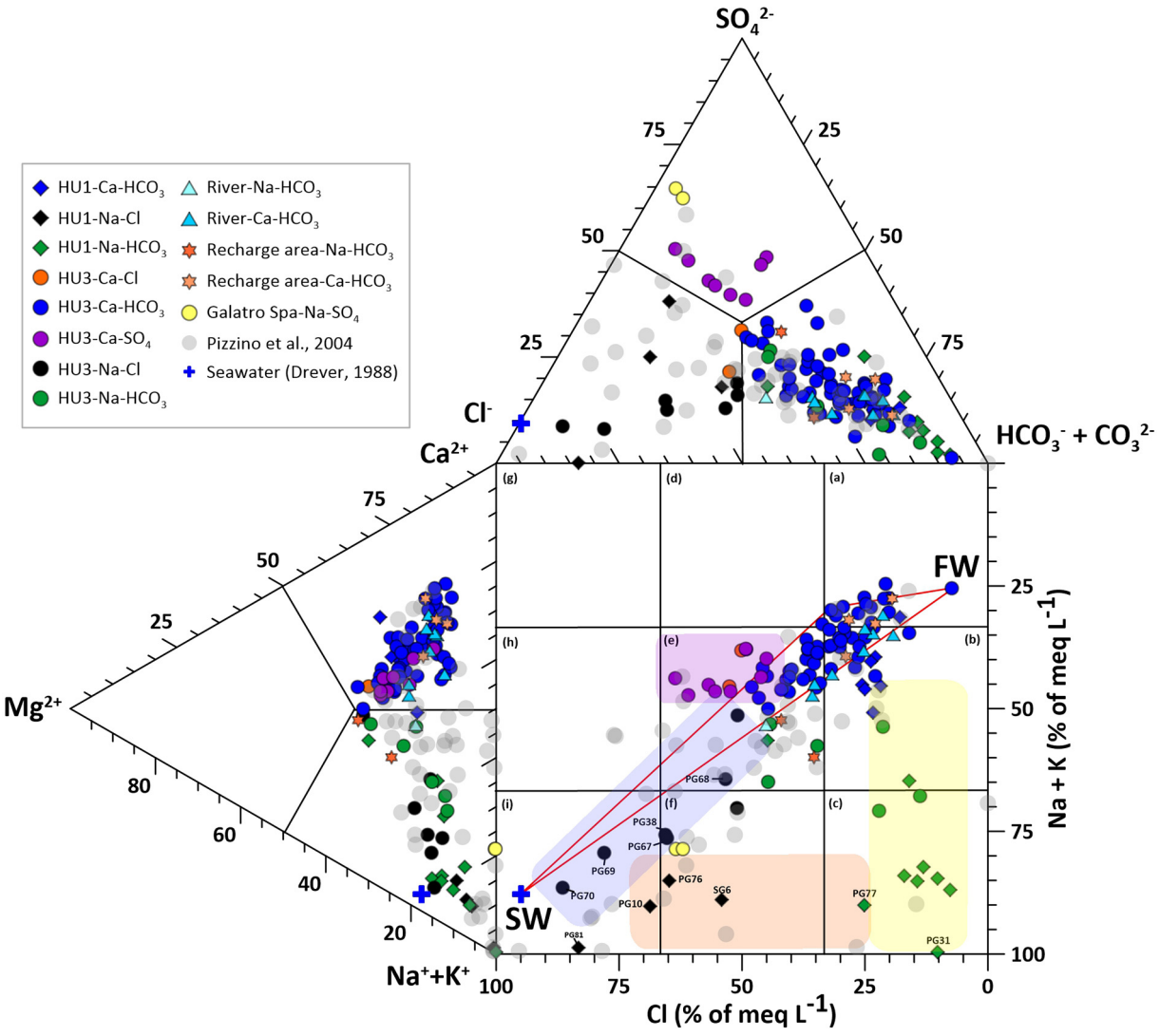

Fig. 2. Durov diagram showing the GTP water facies. Differences from the Ca-HCO_3 type are highlighted by colour shading, namely: yellow for Na-HCO_3 of sectors B, C, D and F; orange for Na-HCO_3(Cl) to Na-Cl of sector B; lilac for Na-Cl waters of sector E (Scinà area); and purple for Ca-SO_4 and Ca-Cl waters of sector C. FW and SW represent freshwater and seawater, respectively.

intrusion, a salinity increase affects the aquifer, and the following exchange reaction takes place:

$$Na^+ + 0.5Ca - X_2 \rightarrow Na - X + 0.5Ca^{2+} \quad (1)$$

where X indicates the cation exchanger. In the reaction, Na^+ is taken up by the exchanger, while Ca^{2+} is released to the aqueous solution. Since no reaction involves Cl^-, water composition changes from Na-Cl to Ca-Cl.

During the freshening processes, the reverse reaction of Eq. (1), induced by freshwater recharge, takes place. The cation exchanger adsorbs Ca^{2+} while Na^+ is released to the aqueous solution with the consequent evolution to the Na-HCO_3 type:

$$0.5Ca^{2+} + Na - X \rightarrow 0.5Ca - X_2 + Na^+ \quad (2)$$

Based on these premises, the analytical cation concentrations of groundwater are commonly used through BEX to identify salinization or freshening tendencies occurring in coastal areas. Several base exchange indices were proposed by different authors as reported by Stuyfzand (2008) who recommended the use of the following:

$$BEX = (Na + K + Mg) - 1.0716\ Cl\ (meq/L) \quad (3)$$

where 1.0716 is the (Na + K + Mg)/Cl ratio in mean ocean water. Thus, the BEX index indicates how much the sum of Na, K, and Mg deviates with respect to the seawater contribution. Nevertheless, such a deviation from the marine cation composition may also be caused by other processes such as mineral dissolution/precipitation reactions (Stuyfzand, 2008). Owing to these uncertainties concerning the BEX index, we decided to ignore the BEX classes and to adopt a simplified code based only on the main type, type, and subtype. The simplified Stuyfzand's classification was used for the straightforward visualization of space trends on cross-sections and maps thanks to the effective and compact coding of the different water facies (Fig. 1a). Finally, the methods of spatial interpolation Inverse Distance Weighting (IDW) and the ordinary kriging, obtained using suitable semi-variogram models to describe the spatial dependence of each parameter, were applied for the generation of isoconcentration maps.

4. Results and discussion

4.1. Physical-chemical parameters

The main statistical indices of the physicochemical groundwater parameters of HU3 and HU1 aquifers are summarized in Table 3S. The GTP groundwaters show a wide range of electrical conductivity (from 228 to

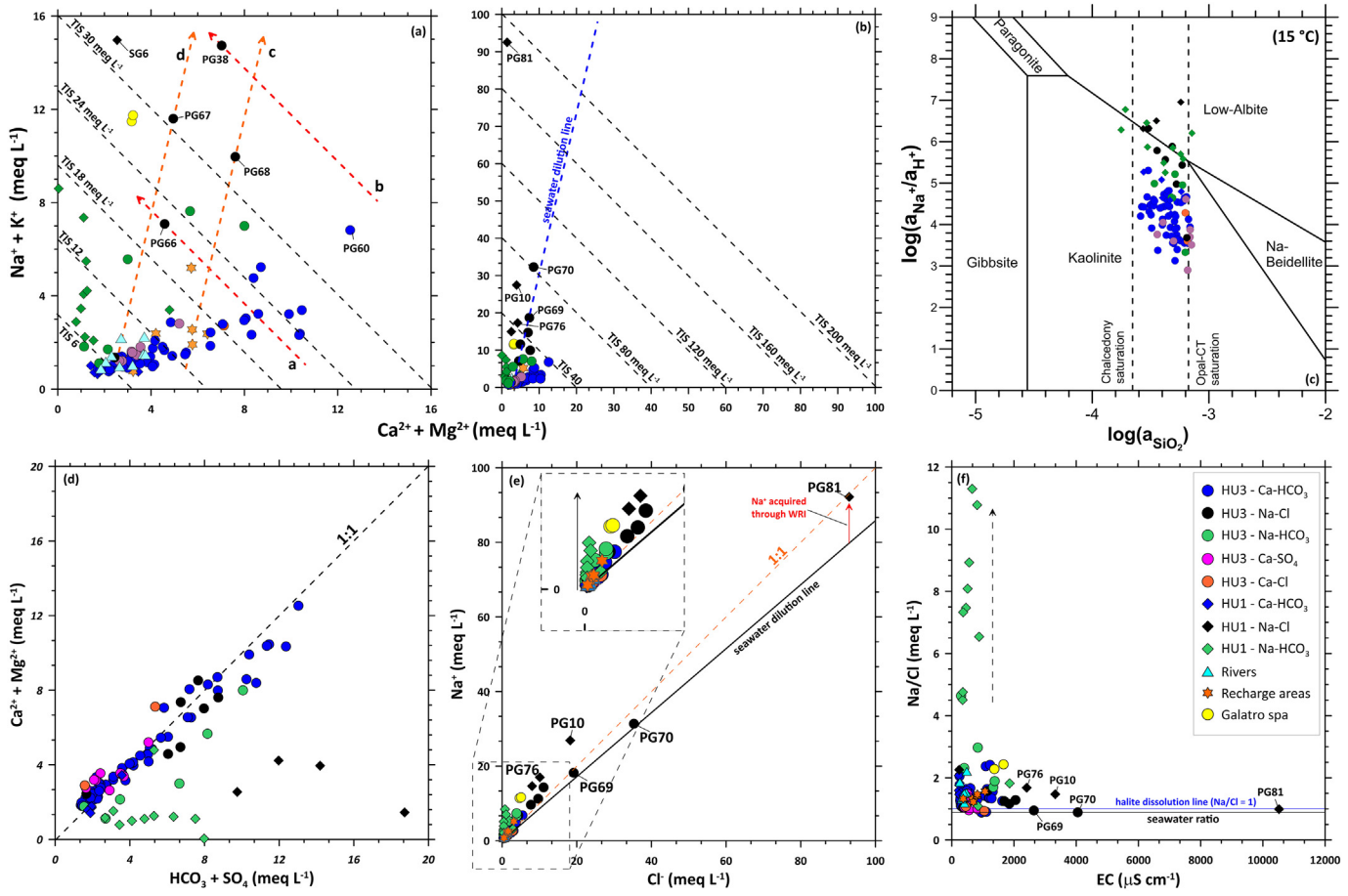

Fig. 3. Correlation diagram of ($Ca^{2+} + Mg^{2+}$) vs. ($Na^{+} + K^{+}$) for (a) low and (b) high salinity samples from the GTP waters. Iso-salinity lines are drawn for reference. Lines a, b, c, and d are discussed in the text. (c) Activity diagram (sensu Helgeson, 1968) showing the stability fields of low-albite, kaolinite, paragonite, gibbsite, Na-beidellite and saturation lines with respect to chalcedony and opal. Binary plots (d) $Ca^{2+} + Mg^{2+}$ vs. $HCO_3^- + SO_4^{2-}$, (e) Cl- vs. Na + and (f) EC vs. Na/Cl showing the water samples from the Gioia Tauro Area.

10,520 µS/cm) indicating that they range from very fresh to very saline, according to Phocaides (2000). The pH from both aquifers exhibits a great variability from north to south of the plain, with values ranging between 5.9 and 8.9. The temperature range is from 14 to 25.8 °C while Eh varies from −250 mV to 300 mV, the negative values mostly related to the HU1 aquifer although, somewhere, Eh values down to −106 mV were also measured in the HU3 groundwaters.

From a general point of view, the main anomalies of the physicochemical parameters are recognized in the northern boundary of the plain (Sector B), along the NGFZ_NW-SE_S, one of the main fault zones dissecting the study area. Waters in this sector show high values of conductivity, pH, and temperature, with pH values > 8 and a peak temperature of 26 °C. Furthermore, the northern sector is characterized by the most negative Eh values when compared to the other areas. The waters from the southern portion of the plain (sector F) are similar to those of the central sectors (C/D), having low conductivity (<1000 µS/cm), positive Eh values and relatively low temperatures (<18 °C). Only one restricted area, along the coastline (Sector E) and confined by the Palmi high (Scinà locality), revealed anomalous conductivity values, >1500 µS/cm.

A significantly different spatial distribution of the physicochemical parameters is shown by the two main aquifers (HU3 and HU1). The 21 samples of deep artesian wells of HU1 (red dots in Figs. 1a and 1Sa) show a spatial heterogeneity much greater than that observed for HU3. The HU1 groundwater shows the highest temperature (mean of 18.6 ± 3.2 °C), highest conductivity (mean of 1224 µS/cm with peaks up to 10,520 µS/cm), and pH (values > 7.5) as well as negative Eh values, with the main anomalies found mainly in proximity of the northern boundary of the plain (Sector *B*). The HU3 groundwater shows mean temperature of 17.4 ± 1.3 °C, variable conductivity values (between 249 and 4049 µS/cm), and pH between 5.9 and 8.5 as well as, in most cases, positive Eh values. In the northern portion of the plain (northward to the Mesima mouth), groundwater of HU3 show relatively high conductivity (EC > 1000 µS/cm) and localized negative Eh values. Nevertheless, the main anomaly (EC > 1500 µS/cm) in HU3 occurs in the south-west (sector E), close to Scinà (Fig. 1a). Finally, the middle and inner portions of the plain (around Rizziconi, Taurianova and Polistena villages), display the lowest temperature and electrical conductivity values.

The physicochemical parameters of main rivers (Budello, Mesima, Metramo and Petrace Rivers) are in most cases similar to those shown by HU3 groundwater. River waters have mean temperature of 15.1 ± 2.9 °C, mean electrical conductivity of 393 ± 79 µS/cm, pH between 7.2 and 8.7 and positive Eh values. Regarding the recharge area, the Capo Vaticano High (PG16, PG17, SG4 and PG71), Palmi High (PG94) and Aspromonte/Serre Massif (PG36) groundwaters differ from the HU1, HU3 groundwater and surface waters due to the distinct lithological-structural framework. These samples were collected close to the GTP outer boundaries, where the groundwater may have undergone a water-rock interaction extent higher with respect to the rainwater infiltrating at high altitudes. Waters from the Aspromonte/Serre Massif show the lowest temperature (14.5 °C) and electrical conductivity (364 µS/cm) values and have relatively high pH (7.9), whereas waters from the Capo Vaticano High (San Giovanni Basin) have electrical conductivities up to 1068 µS/cm and pH between 7.1 and 7.3. Finally, the Palmi High (southern sector) water has an electrical conductivity of 655 µS/cm and a pH of 6.8, i.e., the lowest one among the three recharge areas.

4.2. Water classification

According to the Durov plot (Fig. 2), it is possible to distinguish the different geochemical facies that characterize the groundwaters (from HU1, HU3, and recharge area) and surface water.

(i - shallow aquifer). Shallow groundwaters (HU3) are ascribable to five main chemical facies, namely: Ca-HCO_3 (55 samples), Na-HCO_3 (6 samples), Ca-SO_4 (8 samples), Na-Cl (7 samples) and Ca-Cl (2 samples) (Table 1S). Groundwater samples, showing comparable composition with samples of recharge areas (orange stars in Fig. 2), are mainly Ca-HCO_3 since Ca largely prevails over Mg, with a Ca/Mg ratio (in meq L^{-1}) of 3.3 ± 1.4. These chemical characteristics are probably acquired through water-rock interaction between meteoric waters and Ca-rich carbonate minerals, such as calcite and dolomite (Appelo and Postma, 2005; Apollaro et al., 2009, 2013; White et al., 1999), whose dissolution rate is several orders of magnitude higher than silicate minerals (e.g., Marini, 2006 and reference therein). Calcite is present as an accessory phase in granitoid rocks with concentrations varying between 20 and 18,800 mg/kg (average value of 2520 mg/kg; White et al., 1999, 2005). Thus, meteoric waters of the study area rapidly acquire the Ca-HCO_3 composition through dissolution of disseminated calcite present in the crystalline basement (along the recharge areas) and in the sedimentary rocks derived from the erosion of the crystalline basement. The process is indicated by the following reaction:

$$CaCO_{3(s)} + CO_{2(g,aq)} + H_2O \rightarrow Ca^{2+} + 2HCO_3^- \quad (4)$$

An ideal evolution of this process would involve the distribution of points along a horizontal line in Fig. 3a. Instead, Ca-HCO_3 waters also show a gradual increase in Na^+ and K^+ related to the possible concomitance of secondary processes such as the interaction with crystalline rocks, anthropogenic inputs, and ionic exchange reactions but it is difficult to understand which of these processes explain(s) the enrichment in alkali ions of Ca-HCO_3 waters. Ionic exchange reactions (1) and (2) are described by isosalinity trends and account for the isosalinity evolution from the Ca-HCO_3 to the Na-HCO_3 facies.

The Ca-HCO_3 waters from HU3 are mainly found in the eastern portion of the plain (Sector *A* – Fig. 1Sb) but they are the dominant type of the shallow aquifer (70 %). This type shows low but variable electrical conductivity, between 249 and 1622 μS/cm (from oligohaline [g] to fresh-brackish [f] waters), with the highest value recognized in proximity of the GTP northern boundary (Sector *B*).

The north-central portion of the GTP (Sector *C*), where the inland field of dunes crops out, is characterized by the presence of Ca-SO_4 waters. This chemical type has relatively low conductivity, between 400 and 825 μS/cm (Fresh [F]) and exclusively pertain to HU3. Given the absence of gypsum- or anhydrite-bearing evaporites in the study area, this chemical type could be linked to local anthropic factors or oxidative pyrite dissolution (Rickard, 2012; Rickard et al., 2017) followed by calcite dissolution (the processes controlling the development of the different chemical types will be discussed in depth in the next section).

The Na-HCO_3 waters from HU3 occur in the northern (Sector *B,* between 0.9 and 1.6 km away from the coastline) and south-central parts (Sector *D,* between 1 and 9 km away from the coastline) of GTP close to Nicotera Marina and Budello River, respectively (Fig. 1a). In the northern sector, the Na-HCO_3 samples from HU3 (PG47 and PG75) reflect the composition and the relatively high salinity recognized in the local recharge water. In fact, waters from the Capo Vaticano High (e.g., PG17 representative of the San Giovanni Basin) show high conductivity values when compared with those from the eastern (Aspromonte/Serre) and southern (Palmi High) recharge areas, respectively. On the other hand, for the Na-HCO_3 waters from HU3, collected close to Budello River (Sector D), a distinction between low and relatively high conductivity (from 299 up to 835 μS/cm, respectively) waters is to be made. The low-salinity waters show high Ca/F molar ratio (up to 27) and are undersaturated in calcite. These characteristics are typical of immature waters deriving from the Na-Cl rain waters which are typically found in coastal areas and can be considered strongly diluted seawater (Appelo and Postma, 2005). The evolution from this meteoric composition (very low-TIS G-Na-Cl) to the low-TIS G/g-Na-HCO_3 facies occurs through limited water/rock interaction with the upstream crystalline-metamorphic successions (Fuoco et al., 2022). In contrast, the higher salinity samples show oversaturation with respect to calcite and a lower Ca/F molar ratio (11.5), suggesting a prolonged water/rock interaction with crystalline-metamorphic rocks (Fuoco et al., 2022; Apollaro et al., 2015). Consequently, the overall geochemical evolution can be schematized as: very low TIS G-Na-Cl → low-TIS G/g-Na-HCO_3 → g/F-Ca-HCO_3 → relatively high-TIS F-Na-HCO_3 (Fuoco et al., 2022). However, the occurrence of freshening processes cannot be excluded since during direct cation exchange, calcium concentration decreases favouring the dissolution of F-rich phases (e.g., fluorite) or F-bearing minerals (e.g., apatite, muscovite, and amphibole), leading to a low Ca/F molar ratio (Chen et al., 2020).

The Ca-Cl composition was only identified in two wells from Nicotera Marina (PG74) and close to Rizziconi (PG99). Generally, the chemical Ca-Cl type is mostly due to marine ingression and subsequent cation exchange, according to reaction (1). Nevertheless, both samples represent isolated cases located at different distances from the coast (2 km and 10 km, respectively). For the former an anthropogenic source can be hypothesized. Sample PG74 is indeed localized in proximity of a water treatment plant for drinking water purposes and could account for the anomalous release of Na-Cl waters into the HU3 aquifer. Furthermore, other wells located between PG74, and the coastline typically show a Ca-HCO_3 compositions. Regarding sample PG99, the distance from the coast (10 km) allows to exclude any ion exchange processes linked to seawater intrusion. In this sample, the low Cl/Br molar ratio confirms anthropogenic contamination (see *Section 4.4*). Finally, the Na-Cl group (samples PG38, PG66, PG67, PG68, PG69 and PG70) is mainly found in the southern coastline (Sector *E*), in proximity of Scinà. These samples, as highlighted in Fig. 3a and b, show the highest conductivity values, between 1144 and 4049 μS/cm (from Fresh [F] to brackish-salt [b]), in the shallow aquifer. In particular, samples PG38, PG66, PG67, and PG68 could be produced through either seawater addition to low-salinity Ca-HCO_3 waters or ionic exchange according to reaction (2) involving Ca-HCO_3 waters of higher salinity, as indicated by lines c, d and a, b, respectively (Fig. 3a). Nevertheless, the chemical composition of PG69 and PG70 is unlikely to be related to ionic exchange as it would have involved Ca-HCO_3 waters characterized by very high salinities, much greater than the observed values. Since these two samples lie close the seawater dilution line (Fig. 3b - data from Drever, 1988), it is possible to suggest the presence of direct seawater intrusion, though at a relatively low degree.

(ii - deep aquifer). Deep groundwater (HU1) (represented by diamonds of different colour in Fig. 2) can be divided into three distinct groups, as follows: Ca-HCO_3 (7 samples), Na-HCO_3 (10 samples), and Na-Cl (4 samples) (Table 1S). The Ca-HCO_3 waters, with a Ca/Mg ratio (in meq L^{-1}) of 1.82 ± 0.27, show very low salinity (oligohaline waters [g]) and are mainly found along the southern and eastern boundary of the plain, that is, in sectors *F* and *A*. The Na-HCO_3 waters have low concentrations of Cl^- (<105 mg/L), Ca^{2+} (<45 mg/L), and Mg^{2+} (<30 mg/L). This group of waters represents the dominant facies of HU1 (48 %) characterized by intermediate conductivity, between 350 and 878 μS/cm (from oligohaline [g] to fresh [F] waters) and is well distributed along the southern, central and northern portions of the study area (Sectors *B*, *C*, *D* and *F*). Freshening processes generally control this facies in coastal areas, mainly for the cation exchange reaction (2) (Appelo and Postma, 2005). However, the Na-HCO_3 waters of low salinity can be produced by relatively prolonged interaction between meteoric water and sedimentary rocks deriving by the dismantle of crystalline rocks, governed by the conversion of CO_2 to HCO_3^- in confined aquifers where the residence time of water is comparatively long. The process is schematically represented by the incongruent dissolution of albite, accompanied by precipitation of kaolinite and possibly a silica mineral (Garrels, 1968):

$$NaAlSi_3O_{8(s)} + CO_{2(g,aq)} + 3/2\ H_2O \rightarrow Na^+ + HCO_3^- + 2\ SiO_{2(aq,s)} + 1/2\ Al_2Si_2O_5(OH)_{4(s)}. \quad (5)$$

If albite dissolution occurs at undersaturation conditions with calcite, the concentrations of Na^+ and HCO_3^- are expected to increase in a 1:1 ratio, as dictated by reaction (5). In contrast, if albite dissolution is accompanied by calcite precipitation, then the following reaction would take place:

$$NaAlSi_3O_{8(s)} + 1/2\ CO_{2(g,aq)} + H_2O + 1/2\ Ca^{2+} \rightarrow Na^+ + 1/2\ CaCO_{3(s)} + 2\ SiO_{2(aq,s)} + 1/2\ Al_2Si_2O_5(OH)_{4(s)}. \quad (6)$$

Reaction (6) implies constancy of HCO_3^- concentration and the sum of (Ca^{2+} + Na^{2+}) concentrations in meq L^{-1}. This means that the process is undistinguishable from direct cation exchange, that is, reaction (2). If so, ionic exchange and relatively prolonged dissolution of silicate minerals would virtually produce overlapping effects that are difficult to be discerned. Nevertheless, rock dissolution requires participation of low-salinity Ca-HCO_3 waters (in line with the available evidence), whereas ionic exchange necessitates the involvement of Ca-HCO_3 waters of progressively higher salinity, which were not found in HU1. As shown in Table 1S, almost all Na-HCO_3 waters are in equilibrium or slightly oversaturated with respect to calcite. This makes it further complex to distinguish between the two processes. To provide further details, the decimal logarithms of the Na^+/H^+ activity ratio and the decimal logarithm of SiO_2 activity are plotted into the activity diagram of Fig. 3c. This stability diagram was preferred to relevant saturation indices because analytical Al concentrations may be affected by incomplete removal of suspended colloidal particles and thermodynamic data on Al-bearing solid phases are controversial (e.g., Cioni and Marini, 2020). The HU1 Na-HCO_3 waters fall in the low-albite stability field or close to the boundary separating the kaolinite and low-albite stability fields, thus indicating a greater evolution degree compared to the Ca-HCO_3 waters and the possible occurrence of reaction (6) at saturation state with calcite. Although this evidence is not conclusive, if the Ca^{2+} − Na^+ exchange were controlled by freshening there would be no reason to find water samples close to the kaolinite/low-albite boundary. The origin of this specific chemical type (Na-HCO_3 waters) will be debated in detail in the next section.

Finally, the Na-Cl waters are found in both the outer northern and the southern portions of the plain (Sectors *B* and *F*) and have the highest conductivity values: from 1858 to 10,520 μS/cm (from fresh-brackish [f] to brackish-salt [b] waters). Most Na-Cl HU1 groundwaters have Cl/SO_4 ratio (meq L^{-1}) of 2 ± 0.7, with the exception of sample PG81 (sampled by a 436 m deep well) whose Cl/SO_4 ratio is ~550, possibly due to the occurrence of bacterial sulphate reduction (BSR) under strongly reducing conditions (Marini et al., 2000), as supported by the Eh value (−194 mV). Additionally, as shown in Fig. 3b, the Na-Cl HU1 groundwater is found somewhat to the left of the seawater dilution line, suggesting that the chemical groundwater evolution is different in the two aquifers.

(iii – river water). Surface water of the Budello, Metramo, Mesima and Petrace rivers belong mainly to the Ca-HCO_3 type. This type is typical of freshwater recharge from the northern, southern, and eastern part of the study area. The presence of an isolated Na-HCO_3 water near the Budello river mouth (sample FG1) is probably due to freshening.

(*iv – recharge water)*. Most samples collected in proximity of major recharge areas have Ca-HCO_3 composition and relatively low salinity (g for the Aspromonte/Serre Massifs [PG36] and F for the northern and southern areas). The only exceptions are samples PG17 and PG94, representative of the San Giovanni Basin and Palmi High, respectively, which are Na-HCO_3.

Overall, the Durov square diagram (Fig. 2) reveals that most waters from HU1 and HU3 are positioned in the mixing area connecting the typical (extreme) Ca-HCO_3, NaCl (seawater) and Ca(Mg)-HCO_3 waters, with little or no shifting caused by secondary processes (e.g., direct and inverse cation exchange or prolonged dissolution of silicate minerals). The right and left corner areas in the graph are usually considered representative of fresh water (FW) and seawater (SW), respectively (e.g., Giménez-Forcada et al., 2010; Giménez-Forcada and Sánchez San Román, 2015). Nevertheless, the rain waters in coastal areas are strongly diluted seawater (Appelo and Postma, 2005) and, therefore, they are indistinguishable from seawater in this plot. Since meteoric waters evolve rapidly from initial marine-atmospheric Na-Cl compositions towards Ca-HCO_3 compositions through quick calcite dissolution (see above), sample points move from SW towards FW in the Durov square diagram and not vice versa. Consistent with these expectations, the low-salinity Ca-HCO_3 waters of the GTP are found close to the centre of the Durov square plot, whereas most other Ca-HCO_3 waters are approaching the upper right corner of this plot as salinity increases.

In HU1, 48 % of samples are Na-HCO_3 and positioned along a nearly vertical alignment representative of direct cation exchange or dissolution of Na-Al-silicates and Na-silicates. The Ca-HCO_3 type, recognized in HU1, is characteristic of the eastern and southern boundaries, in proximity of the main recharge areas. These samples, as shown in Fig. 2, fall close to the diagonal line connecting the upper right and the lower left corner areas but they are slightly shifted downward due to either direct cation exchange or dissolution of Na-Al-silicates and Na-silicates. The HU1 waters sampled in proximity of the northern boundary (Sector *B*) fall between the fields (i) and (c) of the Durov square diagram. These waters show relatively high temperature (peak of 26 °C). Their composition is probably conditioned by the NGFZ_NW-SE_S, that favours the uprise of deep Na-Cl thermal waters of high salinity, similar to sample PG81 (Sector *B*), locally intruding the HU1. In the shallow aquifer (HU3), salinization occurring in the southern portion (Scinà Area – Sector *E*) is probably caused by lateral seawater flow from the west. As shown in Fig. 2, the waters samples from the Scinà area fall in proximity of the conservative mixing zone between freshwater and seawater or slightly below it. In this sector, the groundwaters are affected by saltwater intrusion but do not seem to be significantly influenced by inverse cation exchange reaction ($Na^+ \rightarrow Ca^{2+}$) as indicated by the absence of Ca-Cl type waters (*see the next section*). As reported in *Section 2*, Scinà is characterized by a peculiar hydrogeological setting where the shallow aquifer, made by the fluvio-deltaic sediments of the Petrace River and coastal deposits, lies directly in contact with the metamorphic basement. In this framework, the exchangers, necessary for the occurrence of inverse cation exchange and the production of Ca-Cl groundwaters, are expected to be present in small amounts or absent.

4.3. Origin of solutes

The processes controlling the development of the different chemical types is examined by using binary diagrams. Although binary plots involving mobile and conservative species give a partial view of the relationships among the water samples, they can still be useful to verify whether the spread of sample points is consistent with the trends expected for different processes probably occurring during water circulation. In the HU1 and HU3 aquifers relevant processes seem freshening, dissolution of silicate minerals, bacterial sulphate reduction and mineral precipitation. In particular, given the geological framework of the study area, the B, F^- and SiO_2 variability, potentially discriminating species of water-rock interaction with crystalline rocks (Fuoco et al., 2022), was considered. These elements are normally compared with chloride that can be considered a conservative tracer of water evolution (Flury and Prapitz, 1993). Furthermore, chloride concentrations in seawater (ca. 545 meq L^{-1}, Drever, 1988) are significantly higher than those expected in fresh unpolluted groundwater. In this sense, the chloride concentration in the GTP aquifers may be related to either dissolution of Cl-bearing minerals from the aquifer host rocks, mixing with seawater at different degrees or, chloride influx with recharge water (marine aerosols rich in chloride due to sea proximity). Since no Cl-bearing minerals are reported in the reservoir, the climate conditions of the study area (evaporation), connate waters, direct seawater intrusion, and/or the marine aerosols can be identified as the main causes of increasing chloride concentrations.

From a lithological point of view, the GTP basin is filled by siliciclastic and carbonate successions. In this lithological framework, a balance among Ca^{2+}, Mg^{2+}, HCO_3^- and SO_4^{2-} concentrations is expected whenever these solutes are released from dissolution of calcite, dolomite and gypsum (Sarker et al., 2021) and the correlation between (Ca^{2+} + Mg^{2+}) and (HCO_3^- + SO_4^{2-}) is expected to be close to the 1:1 ratio line

(Khairy and Janardhana, 2013; Nasher et al., 2013; Fadili et al., 2015; Sarker et al., 2021). The graphical plot (Fig. 3d) of $(Ca^{2+} + Mg^{2+})^{+}$ vs. $(HCO_3^- + SO_4^{2-})$ shows that most GTP waters belonging to the Ca-HCO_3, Ca-SO_4, Na-Cl, and Ca-Cl water types fall along the 1:1 line. As observed, no sample exhibits Ca^{2+} and Mg^{2+} excess testifying the absence of inverse cation exchange. On the other hand, most Na-HCO_3 waters from HU1 and HU3 are located below the 1:1 line because their HCO_3 concentration is chiefly balanced by Na. This could be due to either direct cation exchange process or occurrence of silicate weathering reactions that also produce an increase of dissolved Na^+ and K^+.

In the Na^+ vs. Cl^- plot (Fig. 3e) most waters fall in proximity of the 1:1 halite dissolution line, apart most Na-HCO_3 waters from HU1 and HU3 that are marked by a Na^+-excess. These waters being positioned above the halite dissolution and seawater dilution lines because their Na^+ concentration is chiefly balanced by HCO_3^-. The departure of the Na-HCO_3 waters from the halite and seawater dilution lines is even more evident in the plot of the Na/Cl ratio vs. EC (μS/cm) (Fig. 3f) in which most samples fall close to the halite dissolution and seawater dilution lines, indicating a direct mixing with seawater in controlling the Na/Cl ratio.

The HU3- and HU1-NaCl waters have different Na/Cl ratios (Fig. 3e). While HU3 NaCl groundwater falls across the seawater dilution line, testifying a direct seawater intrusion, the HU1 NaCl samples are positioned above the seawater dilution line, highlighting ratios comparable to those recognized in the Galatro thermal groundwater. Only sample PG81 (B-NaCl, sector B), in HU1, falls along the 1:1 Na/Cl line. The location (5 km far from the coast) and depth (> 430 m) of PG81 and the absence of evaporitic successions (halite) in the GTP suggest a possible origin linked to a mixing with old connate waters entrapped during the marine transgression.

The HU1- and HU3-NaHCO_3 waters show a positive shift of the Na/Cl ratio at relatively low and comparable salinity, testifying the presence of secondary processes increasing Na^+ concentration. With the aim to improve the knowledge about the main processes able to explain the evolution towards Na-HCO_3 compositions, and the origin of the brackish waters sampled in the northern side (sector *B*), mass balance calculations were carried out on the PG81 brackish water. The $Na_{marine\text{-}derived}$ concentration, i.e., the concentration expected if mixing with seawater were the only process able of providing Na^+ to solution, was calculated considering the $Cl_{measured}$ concentrations (obtained in this study) and those of Cl_{SW} and Na_{SW} representative of average seawater (Drever, 1988):

$$C_{i,marine-derived} = \left(C_{i,SW}/Cl_{SW}\right)^{*}Cl_{measured}. \quad (7)$$

where C_i is the concentrations of i-th component.

The $Cl_{measured}/Na_{marine\text{-}derived}$ ratio (92.97/79.77 = 1.165 in equivalent unit) is consistent with the mean seawater ratio (1.166 in equivalent unit) as shown in Fig. 3e. Therefore, it can be inferred that direct exchange processes do not take place in the brackish water PG81. Thus, the increase in Na^+ is likely due to water-rock interaction processes with the rocks of the crystalline units. Accordingly, the Na concentration derived through dissolution of silicate minerals, Na_{WR}, was calculated as the difference between the analytical value ($Na_{measured}$) and $Na_{marine\text{-}derived}$. The Na_{WR} turned out to be 12.39 meq L^{-1}, which corresponds to the length of the red arrow in Fig. 3e, whereas the corresponding Ca_{WR} (difference between $Ca_{measured}$ and $Ca_{marine\text{-}derived}$) resulted to be −2.59 meq L^{-1} which is obviously meaningless because concentrations cannot be negative. The negative Ca_{WR} value is probably due to the occurrence of calcite precipitation before sampling. Accepting this explanation, the initial (before calcite precipitation) Ca and HCO_3 concentration are at least 3.49 and 21.14 meq L^{-1} (for Ca_{WR} = 0) instead of the analytical counterparts (0.9 and 18.55 meq L^{-1}, respectively). In the correlation diagram of Fig. 4a:

(i) the HU1-Ca-HCO_3 and HU3-Ca-HCO_3 waters are distributed along a horizontal trend, as expected based on reaction (4);
(ii) the HU1-NaHCO_3 and HU1-NaCl waters (including sample PG81 corrected for the effect of calcite precipitation) are situated along a vertical trend and the HU3-Na-HCO_3 waters occupy intermediate positions consistent with the acquisition of Na^+ and the corresponding loss of Ca^{2+} as exemplified by reaction (6).

Based on the above considerations and given the distribution of the Na-HCO_3 waters in both HU1 and HU3, even found at distances of several km from the coast, we can conclude that most Na-HCO_3 waters acquire alkaline elements (chiefly Na^+) by prolonged water-rock interaction with crystalline rocks and/or sediments derived from their erosion. As already mentioned, the evolution of this process is represented by lines of slope − 1 in Fig. 4a, which are representative of a Ca-Na exchange process at constant salinity. In many natural systems, after achieving the saturation condition with respect to carbonate phases (primarily calcite), the dissolution of silicates (mainly feldspars and micas), governed by the conversion of CO_2 to HCO_3^-, indeed occurs with calcite precipitation and results in the transition from the Ca-HCO_3 to the Na-HCO_3 facies at nearly constant salinity (e.g., Pastorelli et al., 2001 and reference therein).

However, the F^- vs. SiO_2 diagram (Fig. 4b) indicates how the discrimination of pure water-rock interaction with crystalline rocks from ion-exchange processes is far from simple to be recognized. It should be noted that fluoride is likely to have a quasi-conservative behavior in the waters under investigation, since all samples are undersaturated with respect to fluorite (Table 1S). The diagram of Fig. 4b suggests that Na-HCO_3 samples are controlled by the three distinct endmembers A, B, and C, whose characteristics are as follows:

- Endmember A has high F (~1.7 mg/L) and low SiO_2 (~ 6 mg/L) and is probably related to direct ion exchange, which favours the decrease in calcium, thereby increasing the solubility of fluorine-rich phases (Chen et al., 2020).
- Endmember B has high F (~2 mg/L) and high SiO_2 (~45 mg/L) and is probably related to direct water-rock interaction with crystalline rocks (Fuoco et al., 2022). Furthermore, the occurrence of volcanoclastic pumice-rich deposits was reported in GTP (De Rosa et al., 2008). These lithotypes typically contain F-bearing minerals acting as F-sources (Dharmagunawardhane et al., 2016). Moreover, the samples richer in endmember B have the highest boron concentrations (Fig. 4c) which are also typical of waters interacting with volcanoclastic deposits (Dharmagunawardhane et al., 2016).
- Endmember C has slightly high SiO_2 (~37 mg/L) and very low F and is probably related to limited water-rock interaction processes with crystalline rocks or mixing with Ca-HCO_3 and SiO_2-rich waters.

The different F/SiO_2 ratios are possibly suggesting the presence of different recharge areas. If, on one hand, the evidence confirms the presence of a water-rock interaction process with crystalline units and/or volcanoclastic deposits (high F, B and SiO_2 concentration and Na-HCO_3 waters recognized in the recharge areas), on the other hand, it is not justified to exclude a priori the presence of the cation exchange process, especially in those samples showing low SiO_2 concentrations.

In the diagrams of Fig. 4d and e, some Ca-HCO_3 samples from HU3 show a positive HCO_3 shift with respect to the 1:1 and local mixing lines. These samples are localized in the northern portion of the study area (sector *B*) which is characterized by several peat levels (Cianflone et al., 2021). Furthermore, the waters have negative Eh values, typical of a reducing environment, which is favourable for the occurrence of the bacterially mediated sulphate reduction through the following reaction (Seal, 2006; Vespasiano et al., 2014):

$$2CH_2O + SO_4^{2-} \rightarrow H_2S + 2HCO_3^- \quad (8)$$

where CH_2O is representative of organic matter (e.g., Berner and Berner, 1996; Stumm and Morgan, 1996; Fidelibus, 2003; Barker et al., 1998; De Montety et al., 2008), although the organic substances actually involved in this process might have a chemical composition other than CH_2O thus leading to a reaction stoichiometry different from that of reaction (8), as

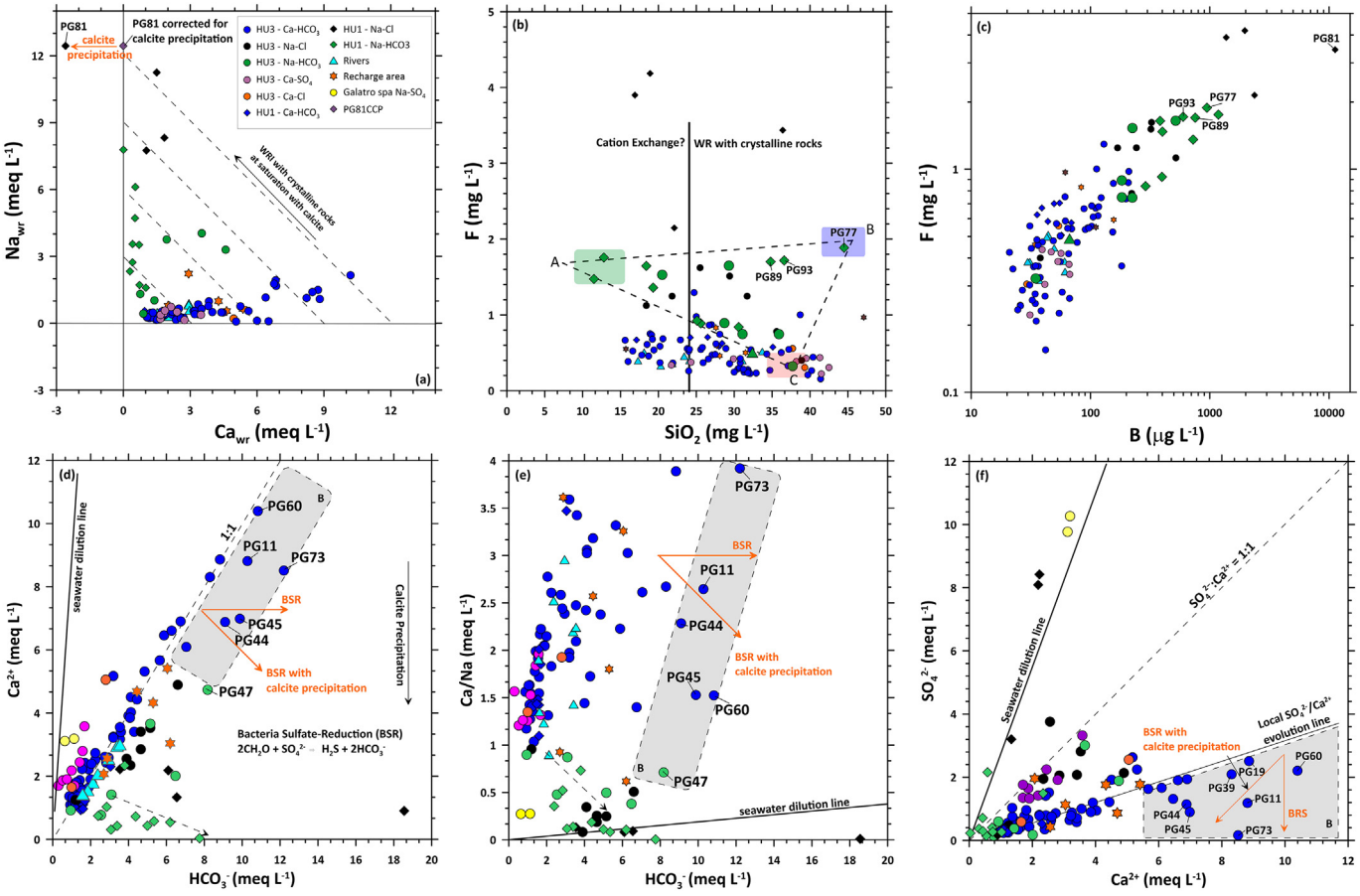

Fig. 4. Binary plots (a) Ca_{wr} vs. Na_{wr}, (b) SiO_2 vs. F, (c) B vs. F, (d) HCO_3 vs. Ca, (e) HCO_3 vs. Ca/Na and (f) Ca vs. SO_4 showing the water samples from the Gioia Tauro Area. BSR: Bacterial Sulphate Reduction. PG81CCP: corrected for calcite precipitation.

discussed by Marini et al. (2000). Irrespective of the stoichiometry of the BSR reaction(s) actually occurring, the BSR process determines a decrease of dissolved sulfate and a corresponding increase of sulfide species (which are usually removed from the aqueous solution, at least partly, through H_2S degassing and/or pyrite precipitation) as well as an increase of dissolved carbonate species (mainly HCO_3, in most cases), often triggering calcite precipitation and a consequent loss of dissolved Ca. In the SO_4^{2-} vs Ca^{2+} diagram (Fig. 4f), the samples affected by BSR and possibly calcite precipitation as well (situated in the grey area) are positioned below the local SO_4^{2-}/Ca^{2+} evolution line confirming the occurrence of these processes. Furthermore, the SO_4^{2-} versus Ca^{2+} plot shows that all water samples, both from the shallow and deep aquifers, have SO_4^{2-}/Ca^{2+} ratio < 1, with the exception of the Ca-SO_4 waters from HU3, which are slightly below the $SO_4^{2-}/Ca^{2+} = 1$ line. For these samples, gypsum dissolution was rejected since there is no evidence of gypsum in the aquifer matrix and the sulfate vs. calcium plot indicated an evolution that could not be easily explained by the dissolution of this phase, but it is more likely attributable to anthropogenic factors (see below).

4.4. Anthropogenic and deep hot systems impact on water chemistry

The Cl/Br ratio has successfully been used to distinguish between various sources of anthropogenic and naturally occurring pollutants in groundwater (Alcalá and Custodio, 2008; Chien and Lautz, 2018). Due to the conservative behavior of Cl and Br ions, insights on the sources affecting the groundwater systems can be highlighted when peculiar Cl/Br ratios are evidenced. The ocean has a constant molar Cl/Br ratio of 650 (Drever, 1988), which is slightly lower than the local Tyrrhenian value (790 ± 90) recognized along the Sicilian coast (Deias unpublished data). Coastal rainfall shows a similar Cl/Br ratio due to the Cl^- and Br^- input along the wind path from the ocean. Inland rainfall (especially in semi-arid and arid areas) may have relatively lower Cl/Br ratios since Cl^- is removed by deposition of cyclic salts in coastal areas (Davis et al., 2001; Edmunds, 2001). Halite dissolution would result in high Cl/Br ratios (up to 1000), as Br^- does not enter the halite lattice during seawater evaporation (Cartwright et al., 2006). The interaction of groundwaters with Cl-bearing contaminants such as domestic wastewater and fertilizers may also give a high Cl/Br signal, as well as the decay of Cl-bearing organic compounds, while the degradation of Br-bearing organic substances may reduce Cl/Br ratios (Flury and Prapitz, 1993).

Bromide concentrations in the GTP aquifers range from 0.0002 to 0.14 meq L^{-1}, and are significantly correlated with chloride, with all the groundwater samples situated along the theoretical seawater mixing line or relatively close to it (Fig. 5a). The strong correlation observed between Br^- and Cl^- is less evident for those samples characterized by low salinity, suggesting the occurrence of secondary processes or different anthropogenic inputs. As reported by Alcalá and Custodio (2008), anthropogenic processes can modify current or natural relic sources of salinity. In their work, the authors collected several water samples affected by natural and anthropogenic sources and defined six groups of groundwater as a function of the Cl/Br ratio: rainwater, unpolluted old phreatic water, recent phreatic water, polluted phreatic water, saline and hypersaline relic seawater, and water affected by wastewater.

Most GTP samples fall in the "rainwater" group (blue circle in Fig. 5b), which is controlled by a prolonged dry period during the summer and autumn followed by short, intense rainfall events and is characterized by $10 < Cl < 100$ mg/L and Cl/Br ratios slightly below the seawater value. Line I in Fig. 5b is a horizontal evaporation line involving unpolluted rainwater and producing uncontaminated old phreatic water having Cl/Br ratios between 600 and 700 (mol L^{-1}) for Cl concentration between 10 and 100 mg/L. The range of Cl/Br ratios is comparable to that of

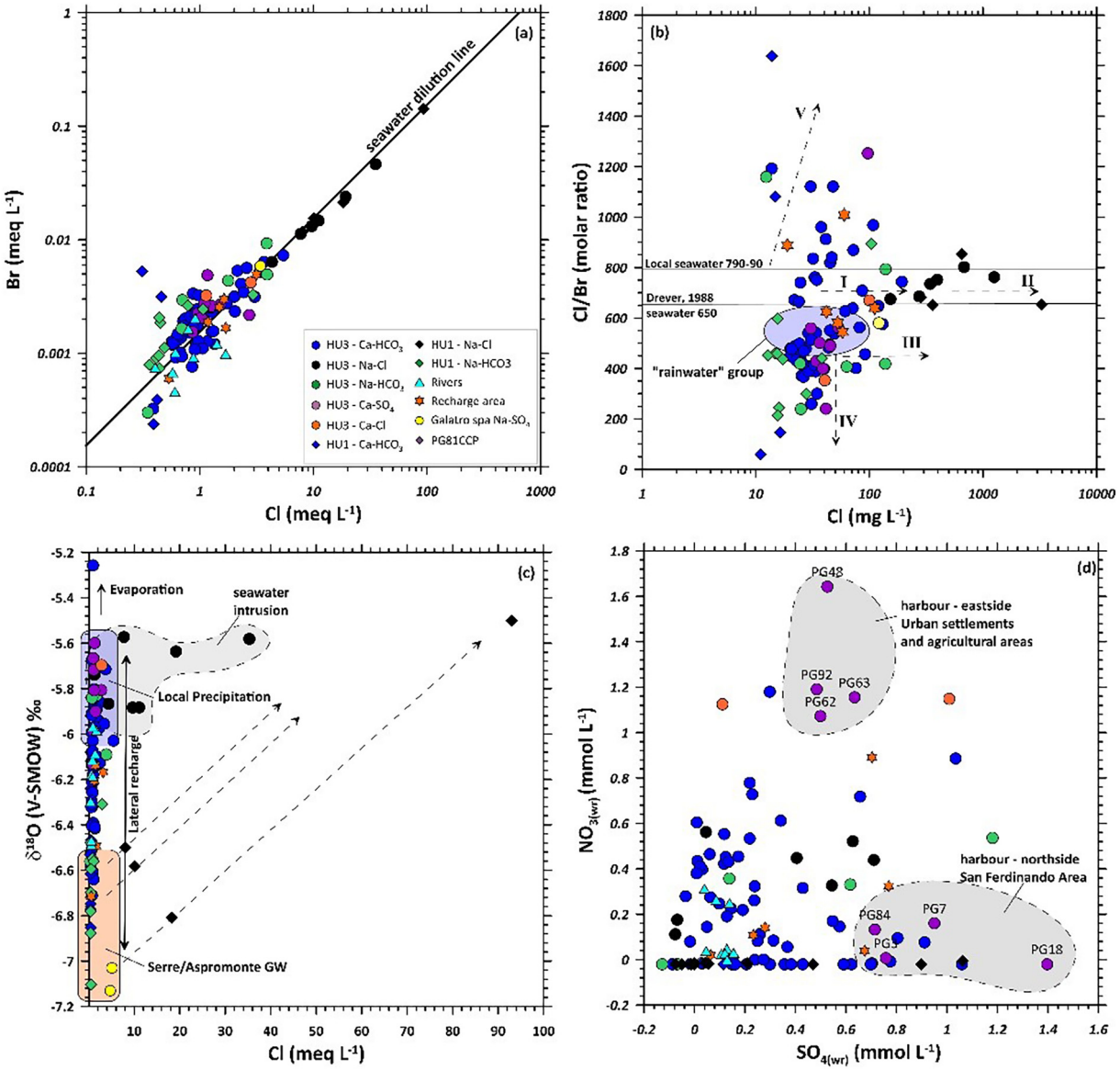

Fig. 5. Binary plots (a) Cl vs. Br, (b) Cl vs. Cl/Br, (c) $\delta^{18}O$ vs. Cl and (d) $NO_{3(wr)}$ vs. $SO_{4(wr)}$ showing the water samples from the Gioia Tauro Area. See the main text for figure details.

seawater and may be explained by decades of airborne marine aerosols from the adjacent coast. Line II is a horizontal mixing line that refers to unpolluted old phreatic waters with salinity derived from unpolluted marine aerosols, and saline and hypersaline relic seawater entrapped in sediments. The relic seawater shows a Cl/Br ratio approaching that of modern seawater. The gradual contribution of unpolluted freshwater to saline and hypersaline relic seawater is concentrated around a horizontal mixing line. Across the line II fall the waters affected by mixing with brackish waters (e.g., connate waters) and direct seawater intrusion including the samples representative of sector E (Scinà). Line III is a horizontal evaporation line starting from present polluted rainwater, with average Cl/Br ratios around 500 (mol L^{-1}), producing phreatic waters with similar Cl/Br ratios. The use of this recent phreatic waters for irrigation only produces evapoconcentration, which does not affect the original Cl/Br ratio of regional bulk deposition. These samples are representative of the GTP areas in which intensive agricultural activities largely occur. Line IV is representative of polluted phreatic waters impacted by Br-based pesticides, as methyl-bromide, e.g., used in sandy areas for soil fumigation in greenhouse. The Cl/Br ratios vary from 500 (mol L^{-1}), like average rainwater, up to values lower than 200 (mol L^{-1}). Most GTP samples and, in particular, the Ca-SO_4 waters of HU3 fall into this group confirming the possible anthropogenic contamination. Finally, the contribution of wastewater from domestic food preparation and cattle feeding increases the Cl/Br ratios up to 1000 (mol L^{-1}) (line V).

The role of the anthropogenic component is further investigated by comparing the values of $\delta^{18}O$ vs. Cl, NO_3/Cl vs. Cl and the calculated nitrate, calcium and sulphate excess in the GTP waters. Their excess represents the difference in concentration, $X_{(wr)}$, between the observed values and those expected if mixing with seawater were the only process (Eq. (7)). As previously stated, the contribution of seawater is derived from the conservative ion Cl^- (Appelo and Postma, 2005).

In Fig. 5c, the two main recharge endmembers characterized by enriched (local coastal rainwater) and depleted (Serre/Aspromonte recharge area) $\delta^{18}O$ values, respectively, are reported. The mixing lines between brackish water and freshwater that cause a shift towards more enriched values in terms of Cl and $\delta^{18}O$ values, are also drawn. HU1 samples are localized in the sector representative of the Aspromonte/Serre massifs recharge, testifying the limited contribution of the local coastal rainfall, while the Ca-SO_4 samples of HU3 fall in proximity of the local rainwater. HU3 Ca-SO_4 samples, localized on the eastern side of the Gioia Tauro harbor, have shown high NO_3 and SO_4 concentration (Fig. 5d). In this sector, agricultural activities, urban settlements and the complete absence of

basic services, such as sewers or connections to aqueducts for domestic use, can favour the increase of these two constituents in solution. In fact, a strong correlation between $NO_{3(wr)}$ vs. $SO_{4(wr)}$ is typically detected in agricultural areas with no other significant salinization processes in act (Menció et al., 2016) because of the application of sulfur and nitrogen fertilizers such as ammonium carbonate [$(NH_4)_2CO_3$] and sulfur-based fungicides (Li et al., 2019). On the other hand, the second group of the HU3 Ca-SO_4 samples, representative of waters collected in the San Ferdinando Area (north side of the harbor), have shown significantly lower NO_3 concentration. However, in both areas, the anomalies are also attributable to the harbor and waste-to-energy power plant SOx emissions which are scavenged by rainwater (Barberi et al., 2021). In fact, in maritime transportation, SOx emissions mainly originate from the combustion of marine fossil fuels (e.g., Tassi et al., 2013), with SO_2 being the most predominant produced oxide. SOx gases can react with oxygen in presence of NO_2 resulting in production of sulfuric acid, which can eventually produce acid rains. The HU3 Ca-SO_4 samples have the lowest pH values (mean value: 6.6, down to 5.9) among the GTP groundwaters, confirming for this chemical type an origin likely linked to anthropic issues, including harbor activities.

The NO_3 concentrations in the GTP waters reach values of 1.66 meq L^{-1}, with 8 % of samples (belonging to HU3) exceeding the law limit values (0.81 meq L^{-1}) according to the D.Lgs. 152/2006 and the World Health Organization drinking water guidelines. The NO_3/Cl ratio vs. Cl plot (Torres-Martínez et al., 2021; Awaleh et al., 2022; Taussi et al., 2022), to distinguish whether NO_3 was derived from agricultural, soil, manure or sewage inputs is represented in Fig. 6a.

The diagram clearly indicates that most HU3 samples align between the agricultural fertilizer and sewage endmember sources, confirming what

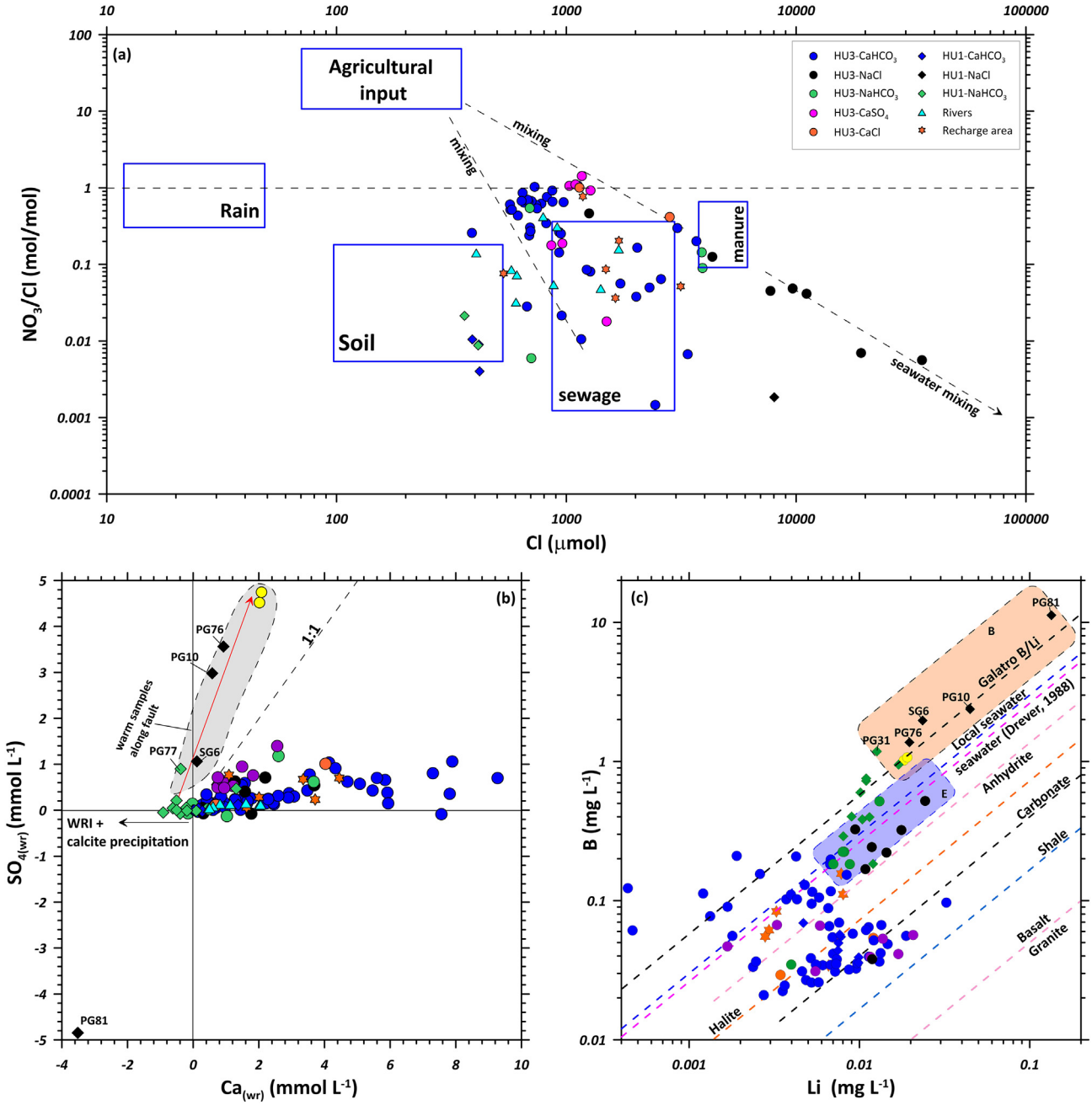

Fig. 6. (a) NO_3/Cl molar ratios versus Cl concentration (in μmol) of the groundwater samples from Gioia Tauro Plain. In the diagram the representative fields of rain, agricultural, soil, sewage, and manure inputs, adapted from Torres-Martínez et al., 2021, Awaleh et al., 2022, Taussi et al., 2022 are reported. Binary plots (b) $Ca_{(wr)}$ vs. $SO_{4(wr)}$ and (c) Li vs. B showing the water samples from the Gioia Tauro Area. See the main text for figure details.

was already highlighted with the Cl/Br ratio. The few HU1 samples, evidencing significant NO_3 concentration fall within the range of the organic soil. Of interest is the right-side of the diagram where the high salinity samples are located. In this area, the samples collected in the Scinà area are arranged along the seawater mixing line (seawater NO_3/Cl molar ratio of 0.0000086 by Drever, 1988) to confirm the ongoing seawater intrusion process.

Finally, among the most controversial samples taken from GTP, the Na-Cl waters from HU1 are characterized by relatively high temperature, up to 26 °C. These samples fall in sector *B*, i.e., close to NGFZ_NW-SE_S. To evaluate the origin of these groundwaters and relevant water-rock interaction processes, the $Ca_{(wr)}$ vs. $SO_{4(wr)}$ values are investigated (Fig. 6b) and the concentrations of B and Li are compared with the overall average composition of minerals and rocks (anhydrite, carbonate, halite, shale, basalt and granite from Turekian and Wedepohl, 1961; Stewart, 1963; Kushnir, 1980; Reimann and De Caritat, 1998) and seawater in Fig. 6c (Drever, 1988; Apollaro et al., 2016).

In Fig. 6b, the HU1 Na-Cl waters fall close to the dilution line of the Galatro thermal site, which is located in the eastern part of the plain along NGFZ_NW-SE_S. Both thermal circuits issue from an enhanced permeability belt closely related to the presence of this regional tectonic line, as claimed by Pizzino et al., 2004. The above-reported trend, not observed in any other samples of the GPT, confirms a direct relationship between the HU1 Na-Cl and the Galatro thermal waters. Finally, the diagram of Fig. 6c shows that B and Li of the GTP waters are chiefly acquired by leaching of carbonate rocks. Immature waters of recharge areas and waters affected by seawater intrusion (Na-Cl waters of HU3 from sector E) fall, as expected, in proximity of the local seawater B/Li ratio. The Na-Cl waters of HU1 are distributed along the dilution line between the Galatro thermal and PG81 waters, corroborating the inferences drawn from the $Ca_{(wr)}$ vs. $SO_{4(wr)}$ diagram (Fig. 6b) and not excluding the contribution of connate waters sampled in sector *B*.

4.5. Fraction of seawater and average recharge altitude estimation

The average infiltration altitude (Hi, m a.s.l.) for the groundwaters of the GTP was calculated by means of the following equation (Vespasiano et al., 2015b):

$$H_{i,^{18}O} = -\frac{\delta^{18}O + 5.25}{0.00210} \quad (9)$$

Results were used to reconstruct the maps of Fig. 3S. The Inverse Distance Weighting (IDW) method of spatial interpolation, often used in Geographical Information System applications, is applied for the generation of this infiltration altitude map. In proximity of the Mesima River mouth and the upstream portion of the Budello River, anomalously high average infiltration altitudes are identified (>150 m), probably due to water exchanges between the rivers (locally affected by evaporation) and the adjacent portions of the shallow aquifer and/or the shallow and deep aquifers. These values were not considered in the reconstruction of the distribution maps. As shown in Fig. 3S, HU1 and HU3 have different infiltration altitudes calculated based on the $\delta^{18}O_{GW}$ value (see below). HU3 is characterized by a constant decrease in infiltration altitude, from ~350 to 0 m a.s.l. moving towards the coast, that is, from east to west, as represented by the isoinfiltration line. These infiltration altitudes are likely to be influenced by local rains, i.e., from rainwater infiltrating directly into GTP.

The influence of local precipitation appears to be less important for HU1. In fact, the deep aquifer has virtually constant infiltration altitude values throughout the plain (410 ± 84 m a.s.l.), suggesting that the meteoric recharge is mainly related to the Aspromonte Massif at the contact with the sedimentary filling of the plain.

Average chloride content (21,339 ± 134 mg/kg), $\delta^{18}O$ value (+1.43 ± 0.10 ‰ vs. V-SMOW) and $\delta^{2}H$ value (+8.1 ± 0.4 ‰ vs. V-SMOW) of local seawater have been assessed using the data available for the Ionian Sea (Stenni et al., 1995; Gat, 1996; Pierre, 1999; Schmidt, 1999). Then, the fraction of seawater, x_{SW}, in each mixed groundwater can be computed by solving the chloride mass balance for x_{SW}:

$$x_{SW} = \frac{Cl_{MW} - Cl_{GW}}{Cl_{SW} - Cl_{GW}} \quad (10)$$

where the subscripts MW, GW and SW refer to mixed groundwater, groundwater unmixed with seawater (Cl = 11.04 mg/kg) and seawater, respectively. Then, the isotope balances were solved for δ_{GW}:

$$\delta_{GW} = \frac{\delta_{MW} - \delta_{SW} * x_{SW}}{1 - x_{SW}} \quad (11)$$

thus, obtaining the $\delta^{18}O_{GW}$ and $\delta^{2}H_{GW}$ values of the groundwaters unmixed with seawater (Table 1S). These corrected isotope values (black line in Fig. 7a) define the local meteoric line, which diverges from the Southern

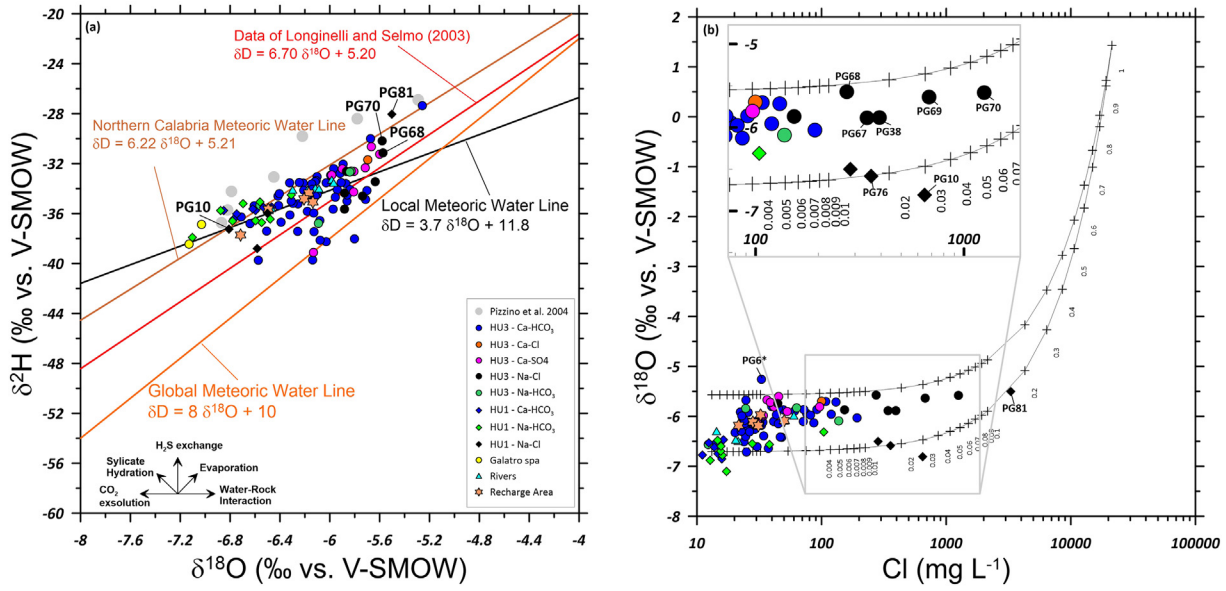

Fig. 7. (a) Diagram of $\delta^{2}H$ vs. $\delta^{18}O$ of GTP water samples and the southern Italy meteoric water line proposed by Longinelli and Selmo, 2003, the northern Calabria meteoric water line (Vespasiano et al., 2015b), the global meteoric water line (Craig, 1961), and the local GTP meteoric water line (black line). (b) $\delta^{18}O$ vs. Cl (mg L^{-1}) for the GTP samples. The two-limiting groundwater-seawater mixing lines and the fractions of seawater in the mixtures are also reported.

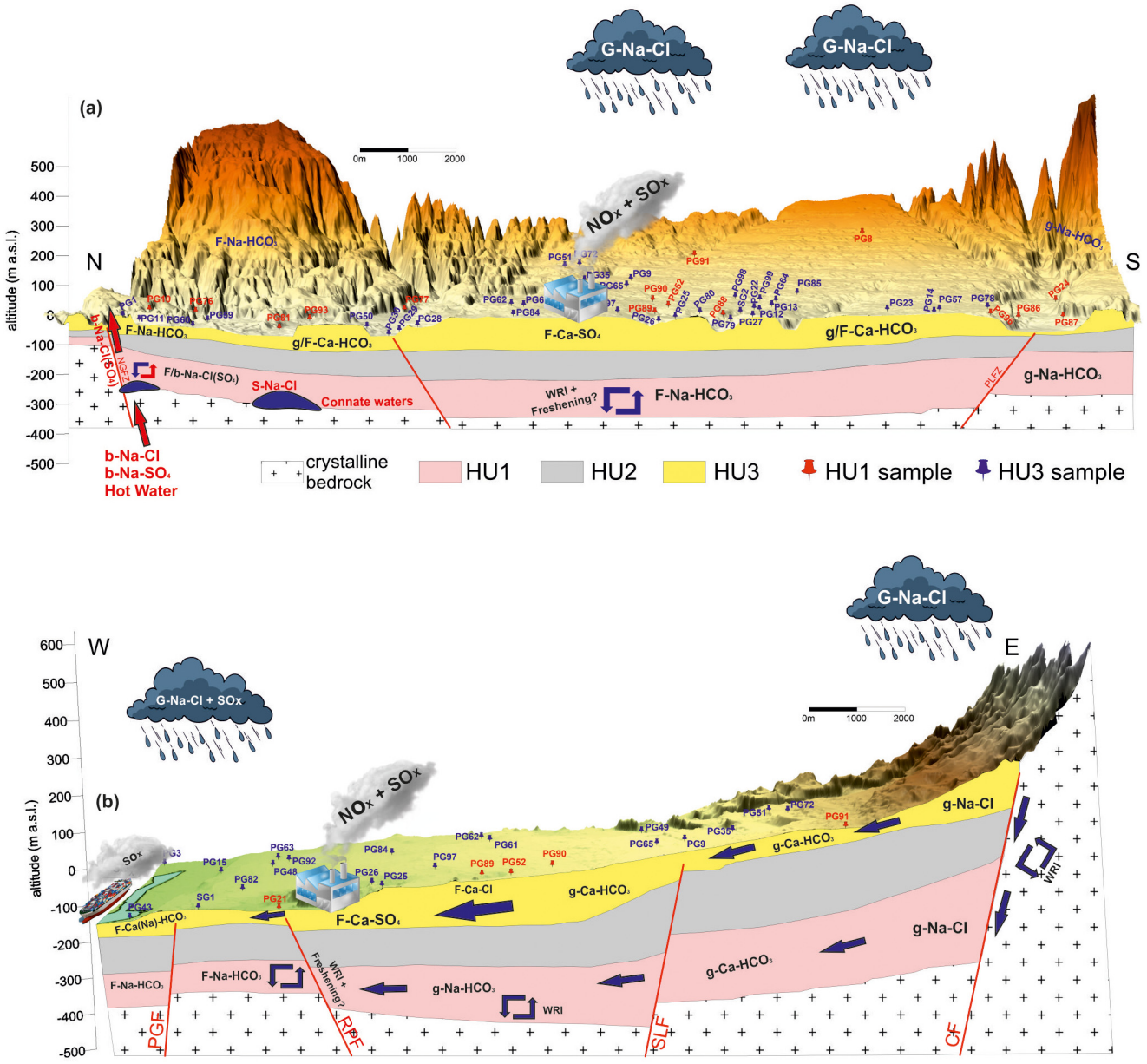

Fig. 8. Graphical visualizations of the conceptual model of the GTP. Blue and red pins represent samples from shallow and deep aquifer, respectively.

Italy (Longinelli and Selmo, 2003; Giustini et al., 2016) and Northern Calabria (Vespasiano et al., 2015b) meteoric lines. Local meteoric waters have much higher d-excess values (Table 1S), attributable to non-equilibrium (kinetic) evaporation at relatively low humidity.

The seawater fractions of local groundwater generally range from 0.1 % to 0.2 %, with peaks between 1 % and 7 % for the samples collected in sector E – Scinà Area (HU3) and about 15 % for sample PG81, which is likely mixed with connate brackish water. As shown in the Cl vs. $\delta^{18}O$ plot (Fig. 7b), the $\delta^{18}O$ values of groundwater span a range of 1.5 ‰ units, attributable to differences in the location and/or altitude of the recharge areas. Evaporative effects are evident for waters collected from wells of large diameter open to the atmosphere and exchanging with it (e.g., PG6).

Finally, the two aquifers HU1 and HU3 have different d-excess values, 17 ± 1.4 ‰ and 13.7 ± 2.6 ‰, respectively (Table 1S), even if the difference between these two values is not significant considering their uncertainty/variability. Pfahl and Sodemann (2014) reported as the relative humidity of the moisture source is the main driver of d-excess variability. The different values of d-excess in HU1 and HU3 could indicate a different moisture source contribution, with greater d-excess values from the east (main recharge area for HU1) and minor d-excess values from the west (influence of local rains for HU3).

5. Concluding remarks

The results of the geochemical survey carried out on 114 samples evenly distributed throughout GTP, combined with relevant hydrogeological data, allow to reconstruct the site-specific conceptual model, graphically represented in Fig. 8a and b and summarized here below.

Two main aquifers were recognized over most of the study area: (i) a shallow aquifer, HU3, hosted in late Pleistocene and Holocene marine and alluvial sediments and (ii) a deep aquifer, HU1, hosted in the late Miocene succession, made up of siliciclastic and carbonate deposits. According to the stable isotopic ($\delta^{18}O$ and $\delta^{2}H$) values, the latter is mostly recharged by local rains whereas the former is apparently less influenced by local precipitation. The two aquifers are separated by the Pliocene clayey and silty deposits acting as an aquitard (HU2). Nevertheless, the deep aquifer is absent in the Scinà area, between the coastline and the Palmi High (Sector

E), where the shallow aquifer (HU3) directly overlies the metamorphic basement.

Deep and shallow aquifers are fed mainly by Ca^{2+}-HCO_3^- waters from the main recharging areas except in localized borders sectors where Na^+-HCO_3^- waters are produced through the interaction of meteoric waters with the crystalline-metamorphic basements. Ca^{2+}-HCO_3^- and Na^+-HCO_3^- waters suffer from secondary processes occurring during their east-to-west migration:

(i) in HU3 inputs of N-rich sewage and agriculture-related contaminants and SOx emissions in proximity of the harbor represent the main processes favouring nitrate increases over almost the entire plain and the evolution towards the Ca-SO_4 composition. Furthermore, BSR processes induced by oxidation of organic matter in sector *B* and groundwater-seawater mixing in sector E represent secondary and localized processes.

(ii) Na-HCO_3 waters of intermediate salinity are the dominant hydro-facies in HU1 with a percentage of 48 %. Mass balance calculations and the distribution of some major and minor constituents (SiO_2, F and B) allow one to identify at least two possible origins for this chemical type: (a) the prolonged water-rock interaction with crystalline rocks and sediments deriving from their erosion, also comprising volcanoclastic deposits and (b) cation exchange processes, for the samples having low SiO_2 concentrations.

Connate waters are present at depth in the study area as indicated by sample PG81, which was collected from a 436-m-deep well drilled in sector *B* and is characterized by Na-Cl composition and high concentrations of Cl (~3300 mg/kg) and B (11 mg/kg), and relatively high Li concentration (0.13 mg/kg). Other two waters also coming from sector *B*, specifically from HU1, samples PG10 and PG76, have Na-Cl composition, relatively high temperature (26 °C), and the same B/Cl and Li/Cl ratios of sample PG81, but significantly lower Cl concentrations, 647 and 358 mg/kg, respectively, due to a larger extent of mixing of the connate water endmember with the low-salinity HU1 groundwaters. These three wells PG81, PG10, and PG76 are found along the important right strike-slip NGFZ_NW-SE_S limiting the GTP to the north (Fig. 1Sa). PG10 and PG76 wells are situated close to a bend of the NGFZ_NW-SE_S, locally creating an extensional regime, which favour the uprising of the deep connate waters and their intrusion in HU1, as observed in the pull-apart basins along the Sumatran fault (Muraoka et al., 2010). Also the Galatro thermal springs (35–38 °C) are found along the NGFZ_NW-SE_S, but they represent the discharge of a distinct thermal circuit, as indicated by their Na(Ca)-SO_4(Cl) chemistry and low Cl concentration (167–180 mg/kg).

Overall, our study revealed that a direct marine intrusion seems to be very localized despite the high demand for water related to the anthropic activities. The growing water requirement is linked to the increase in industrial settlements and to the land use change that happened during the last two decades. In detail, the main change is due to the intensive and ongoing kiwifruit farming that requires a high-water supply (6000–10,000 m^3/ha Holzapfel et al., 2000) compared to the previous citrus and olive crops, with a water consumption of 4000–6000 m^3/ha for citrus crops and almost zero for olive (Food and Agriculture Organization (FAO)). The qualitative and quantitative conditions of the aquifer are kept at acceptable levels due to the high recharge inflow that comes mainly from the Aspromonte massif, where the mean precipitation value is 1274 mm/a. An incipient groundwater-seawater mixing, involving up to 7 % seawater, was only recognized in the SW area (Sector E), in proximity of Scinà.

The obtained results confirm the importance of the multidisciplinary approach to identify and characterize sources and driving mechanisms and produce a reliable conceptual model. These results will provide an important support to the decision-making and management phases of the GTP resources.

Supplementary data to this article can be found online at https://doi.org/10.1016/j.scitotenv.2022.160694.

CRediT authorship contribution statement

G. Vespasiano: Conceptualization, Methodology, Software, Formal analysis, Field investigation, Laboratory analysis, Resources, Data curation, Writing—original draft preparation, Writing—review & editing, Project administration, Funding acquisition.

G. Cianflone: Conceptualization, Methodology, Software, Formal analysis, Field investigation, Laboratory analysis, Resources, Data curation, Writing — original draft preparation, Writing — review & editing, Project administration, Funding acquisition.

L. Marini: Conceptualization, Methodology, Formal analysis, Data curation, Writing — original draft preparation, Writing — review & editing, Supervision.

R. De Rosa: Validation, Writing - review & editing, Supervision, Funding acquisition.

M. Polemio: Validation, Writing — review & editing, Supervision.

K. Walraevens: Validation, Writing — review & editing, Supervision.

O. Vaselli: Formal analysis, Laboratory analysis, Writing—review & editing.

L. Pizzino: Laboratory analysis, Writing—review & editing.

D. Cinti: Laboratory analysis, Writing—review & editing.

F. Capecchiacci: Laboratory analysis.

D. Barca: Laboratory analysis, Writing—review & editing.

R. Dominici: Conceptualization, Formal analysis, Writing—review & editing.

C. Apollaro: Conceptualization, Formal analysis, Data curation, Writing - original draft preparation, Writing - review & editing, Supervision.

Data availability

Data will be made available on request.

Declaration of competing interest

The authors declare that they have no known competing financial interests or personal relationships that could have appeared to influence the work reported in this paper.

Acknowledgement

Giovanni Vespasiano and Giuseppe Cianflone are funded by the POC-AIM 1802990: “Attraction and International Mobility”-Research and innovation, Line 1 (Mobility of researchers). The authors wish to thank Giovanni Andiloro, Vincenzo Tripodi, Jasmine De Marco, Domenico Putrino, Rizziconi and Rosarno municipalities, and Sorical s.p.a. for field assistance and for their support during all work phases. Suggestions and critical comments by the Editor and two reviewers (Dr Claudio Inguaggiato and an anonymous reviewer) greatly helped to improve and clarify the paper.

References

Abu Al Naeem, M.F., Yusoff, I., Ng, T.F., Maity, J.P., Alias, Y., May, R., Alborsh, H., 2019. A study on the impact of anthropogenic and geogenic factors on groundwater salinization and seawater intrusion in Gaza coastal aquifer. Palestine: an integrated multi-techniques approach. J. Afr. Earth Sci. 156, 75–93. https://doi.org/10.1016/j.jafrearsci.2019.05.006.

Alcalá, F.J., Custodio, E., 2008. Using the Cl/Br ratio as a tracer to identify the origin of salinity in aquifers in Spain and Portugal. J. Hydrol. 359 (1–2), 189–207.

Alfarrah, N., Walraevens, K., 2018. Groundwater overexploitation and seawater intrusion in coastal areas of arid and semi-arid regions. Water 10 (2), 143. https://doi.org/10.3390/w10020143.

Alshehri, F., Sattam Almadani, S., El-Sorogy, A.S., Alwaqdani, E., Alfaifi, H.J., Alharbi, T., 2021. Influence of seawater intrusion and heavy metals contamination on groundwater quality, Red Sea coast,Saudi Arabia. Mar. Pollut. Bull. 165, 112094. https://doi.org/10.1016/j.marpolbul.2021.112094.

Apollaro, C., Accornero, M., Marini, L., Barca, D., De Rosa, R., 2009. The impact of dolomite and plagioclase weathering on the chemistry of shallow groundwaters circulating in a granodiorite-dominated catchment of the Sila Massif (Calabria, Southern Italy). Appl. Geochem. 24, 957–979.

Apollaro, C., Marini, L., Critelli, T., De Rosa, R., Bloise, A., Miriello, D., Catalano, M., Armano, V., 2013. Modeling of the impact of dolomite and biotite dissolution on vermiculite composition in a gneissic shallow aquifer of the Sila Massif (Calabria, Italy). Appl. Geochem. 35, 297–311.

Apollaro, C., Vespasiano, G., De Rosa, R., Marini, L., 2015. Use of mean residence time and flowrate of thermal waters to evaluate the volume of reservoir water contributing to the natural discharge and the related geothermal reservoir volume. Application to Northern Thailand hot springs. Geothermics 58, 62–74.

Apollaro, C., Vespasiano, G., Muto, F., De Rosa, R., Barca, D., Marini, L., 2016. Use of mean residence time of water, flowrate, and equilibrium temperature indicated by water geothermometers to rank geothermal resources. Application to the thermal water circuits of Northern Calabria. J. Volcanol. Geotherm. Res. 328, 147–158.

Apollaro, C., Tripodi, V., Vespasiano, G., De Rosa, R., Dotsika, E., Fuoco, I., Critelli, S., Muto, F., 2019. Chemical, isotopic and geotectonic relations of the warm and cold waters of the Galatro and Antonimina thermal areas, southern Calabria, Italy. Mar. Pet. Geol. 109, 469–483. https://doi.org/10.1016/j.marpetgeo.2019.06.020.

Apollaro, C., Buccianti, A., Vespasiano, G., Vardè, M., Fuoco, I., Barca, D., Bloise, A., Miriello, D., Cofone, F., Servidio, A., De Rosa, R., 2019. Comparative geochemical study between the tap waters and the bottled mineral waters in Calabria (Southern Italy) by compositional data analysis (CoDA) developments. Appl. Geochem. 107, 19–33.

Apollaro, C., Caracausi, A., Paternoster, M., Randazzo, P., Aiuppa, A., De Rosa, R., Fuoco, I., Mongelli, G., Muto, F., Vanni, E., Vespasiano, G., 2020. Fluid geochemistry in a low-enthalpy geothermal field along a sector of southern Apennines chain (Italy). J. Geochem. Explor. 219, 106618.

Apollaro, C., Di Curzio, D., Fuoco, I., Buccianti, A., Dinelli, E., Vespasiano, G., Castrignanò, A., Rusi, S., Barca, D., Figoli, A., Gabriele, B., 2022. A multivariate non-parametric approach for estimating probability of exceeding the local natural background level of arsenic in the aquifers of Calabria region (Southern Italy). Sci. Total Environ. 806, 150345.

Appelo, C., Postma, D., 2005. Geochemistry, Groundwater and Pollution. 2nd ed. Balkema, Rotterdam https://doi.org/10.1201/9781439833544.

ARPACAL, ARPACAL,]. Centro Funzionale Multirischi. Consultazione banca dati storici http://www.cfd.calabria.it/index.php?option=com_wrapper&view=wrapper&Itemid=41.

Awaleh, M.O., Boschetti, T., Adaneh, A.E., Chirdon, M.A., Ahmed, M.M., Dabar, O.A., Soubaneh, Y.D., Egueh, N.M., Kawalieh, A.D., Kadieh, I.H., Chaheire, M., 2022. Origin of nitrate and sulfate sources in volcano-sedimentary aquifers of the East Africa Rift System: an example of the Ali-Sabieh groundwater (Republic of Djibouti). Sci. Total Environ. 804, 150072.

Barberi, S., Sambito, M., Neduzha, L., Severino, A., 2021. Pollutant emissions in ports: a comprehensive review. Infrastructures 6, 114. https://doi.org/10.3390/infrastructures6080114.

Barker, W.W., Welch, S.A., Chu, S., Banfield, J.F., 1998. Experimental observations of the effects of bacteria on aluminosilicate weathering. Am. Mineral. 83 (11), 1551–1563.

Barlow, M.P., 2003. Groundwater in Freshwater-Saltwater Environments of the Atlantic Coast. U.S. Geological Survey Circular, Reston, GA, USA.

Barlow, P.M., Reichard, E.G., 2010. Saltwater intrusion in coastal regions of North America. Hydrogeol. J. 18 (1), 247–260.

Barrocu, G., 2003. Seawater intrusion in coastal aquifers of Italy. Tecnología de la Intrusión de Agua de Mar en Acuíferos Costeros: Países Mediterráneos. Instituto Geológico y Minero de España, Madrid.

Bellafiore, D., Ferrarin, C., Maicu, F., Manfè, G., Lorenzetti, G., Umgiesser, G., Zaggia, L., Valle, Levinson A., 2021. Saltwater intrusion in a Mediterranean delta under a changing climate. J. Geophys. Res. Oceans 126, e2020JC016437. https://doi.org/10.1029/2020JC016437.

Berner, E.K., Berner, R.A., 1996. Global Environment: Water, Air and Geochemical Cycles. Prentice Hall, Upper Saddle River.

Bocanegra, E., Da Silva, G.C., Custodio, E., Manzano, M., Montenegro, S., 2010. State of knowledge of coastal aquifer management in South America. Hydrogeol. J. 18, 261–267.

Bompoti, N., Chrysochoou, M., Dermatas, D., 2015. Geochemical characterization of Greek ophiolitic environments using statistical analysis. Environ. Process 2, 5–21. https://doi.org/10.1007/s40710-015-0097-z.

Boughriba, M., Jilali, A., 2018. Climate change and modeling of an unconfined aquifer: the Triffa plain, Morocco. Environ. Dev. Sustain. 20 (5), 2009–2026.

Boumaiza, L., Chesnaux, R., Drias, T., Walter, J., Huneau, F., Garel, E., Knoeller, K., Stumpp, C., 2020. Identifying groundwater degradation sources in a Mediterranean coastal area experiencing significant multi-origin stresses. Sci. Total Environ. 746, 141203.

Brozzo, G., Accornero, M., Marini, L., (011. The alluvial aquifer of the Lower Magra Basin (La Spezia, Italy): conceptual hydrogeochemical–hydrogeological model, behavior of solutes, and groundwater dynamics. Carbonates and Evaporites 26(3), 235-254. n.d.

Bruni, J., Canepa, M., Cipolli, F., Marini, L., Ottonello, G., Vetuschi Zuccolini, M., Chiodini, G., Cioni, R., Longinelli, A., 2002. Irreversible water-rock mass transfer accompanying the generation of the neutral, Mg-HCO3 and high-pH, Ca-OH spring waters of the Genoa province, Italy. Appl. Geochem. 17, 455–474.

Capaccioni, B., Didero, M., Paletta, C., Didero, L., 2005. Saline intrusion and refreshening in a multilayer coastal aquifer in the Catania Plain (Sicily, Southern Italy): dynamics of degradation processes according to the hydrochemical characteristics of groundwaters. J. Hydrol. 307 (1–4), 1–16.

Cardoso, P., 1993. Saline water intrusion in Mexico. In: Brebbia, C.A. (Ed.), Water Pollution. Transactions on Ecology and the Environmentvol. 2. WIT Press, Southampton.

Carreira, P.M., Marques, J.M., Nunes, D., 2014. Source of groundwater salinity in coastline aquifers based on environmental isotopes (Portugal): natural vs. human interference. A review and reinterpretation. J. Appl. Geochem. 41, 163–175. https://doi.org/10.1016/j.apgeochem.2013.12.012.

Carrión-Mero, P., Montalván, F.J., Morante-Carballo, F., Heredia, J., Elorza, F.J., Solórzano, J., Aguilera, H., 2021. Hydrochemical and isotopic characterization of the waters of the Manglaralto River Basin (Ecuador) to contribute to the management of the coastal aquifer. Water 13, 537. https://doi.org/10.3390/w13040537.

Cartwright, I., Weaver, T.R., Fifield, L.K., 2006. Cl/Br ratios and environmental isotopes as indicators of recharge variability and groundwater flow: an example from the Southeast Murray Basin,Australia. Chem. Geol. 231 (1–2), 38–56.

Chen, Q., Jia, C., Wei, J., Dong, F., Yang, W., Hao, D., Jia, Z., Ji, Y., 2020. Geochemical process of groundwater fluoride evolution along global coastal plains: evidence from the comparison in seawater intrusion area and soil salinization area. Chem. Geol. 552, 119779.

Chien, N.P., Lautz, L.K., 2018. Discriminant analysis as a decision-making tool for geochemically fingerprinting sources of groundwater salinity. Sci. Total Environ. 618, 379–387.

Cianflone, G., Dominici, R., Viscomi, A., 2015. Potential recharge estimation of the Sibari Plain aquifers (southern Italy) through a new GIS procedure. Geographia Techica 10 (1), 8–18.

Cianflone, G., Vespasiano, G., De Rosa, R., Dominici, R., Apollaro, C., Vaselli, O., Pizzino, L., Tolomei, C., Capecchiacci, F., Polemio, M., 2021. Hydrostratigraphic framework and physicochemical status of groundwater in the Gioia Tauro Coastal Plain (Calabria—Southern Italy). Water 13, 3279. https://doi.org/10.3390/w13223279.

Cianflone, G., Vespasiano, G., Tolomei, C., De Rosa, R., Dominici, R., Apollaro, C., Walraevens, K., Polemio, M., 2022. Different ground subsidence contributions revealed by integrated discussion of Sentinel-1 datasets, well discharge, stratigraphical and geomorphological data: the case of the Gioia Tauro Coastal Plain (Southern Italy). Sustainability 2926. https://doi.org/10.3390/su14052926.

Cioni, R., Marini, L., 2020. A Thermodynamic Approach to Water Geothermometry. Springer Geochemistry Series. Springer, Cham, Switzerland https://doi.org/10.1007/978-3-030-54318-1.

Cipolli, F., Gambardella, B., Marini, L., Ottonello, G., Vetuschi Zuccolini, M., 2004. Geochemistry of high-pH waters from serpentinites of the Gruppo di Voltri (Genoa, Italy) and reaction path modeling of CO2 sequestration in serpentinite aquifers. Appl. Geochem. 19, 787–802.

Cirrincione, R., Fazio, E., Fiannacca, P., Ortolano, G., Pezzino, A., Punturo, R., 2015. The Calabria-Peloritani Orogen, a composite terrane in Central Mediterranean; its overall architecture and geodynamic significance for a pre-Alpine scenario around the Tethyan basin. Period.Mineral. 84 (3B), 701–749.

Geoportale Nazionale, Ministero dellAmbiente, Modello digitale del terreno - 20 metri. http://wms.pcn.minambiente.it/wcs/dtm_20m. (Accessed 13 March 2022).

Corniello, A., Cardellicchio, N., Cavuoto, G., Cuoco, E., Ducci, D., Minissale, A., Mussi, M., Petruccione, E., Pelosi, N., Rizzo, E., Polemio, M., Tamburino, S., Tedesco, D., Tiano, P., Iorio, M., 2015. Hydrogeological characterization of a geothermal system: the case of the thermo-mineral area of Mondragone (Campania, Italy). Int.J.Environ.Res. 9 (2), 523–534. https://doi.org/10.22059/IJER.2015.926.

Craig, H., 1961. Isotopic variations in meteoric waters. Science 133 (3465), 1702–1703.

Custodio, E., 2010. Coastal aquifers of Europe: an overview. Hydrogeol. J. 18, 269–280.

Davis, S.N., Cecil, L.D., Zreda, M., Moysey, S., 2001. Chlorine-36, bromide, and the origin of spring water. Chem. Geol. 179 (1–4), 3–16.

De Montety, V., Radakovitch, O., Vallet-Coulomb, C., Blavoux, B., Hermitte, D., Valles, V., 2008. Origin of groundwater salinity and hydrogeochemical processes in a confined coastal aquifer: case of the Rhône delta (Southern France). Appl. Geochem. 23 (8), 2337–2349.

De Rosa, R., Dominici, R., Donato, P., Barca, D., 2008. Widespread syn-eruptive volcaniclastic deposits in the Pleistocenic basins of South-Western Calabria. J. Volcanol. Geotherm. Res. 177, 155–169.

Dharmagunawardhane, H.A., Malaviarachchi, K.P.S., Burgess, W., 2016. Fluoride content of minerals in gneissic rocks at an area of endemic dental fluorosis in Sri Lanka: estimates from combined petrographic and electron microprobe analysis. Ceylon J. Sci 45 (1), 57–66.

Drever, J.I., 1988. The Geochemistry of Natural Waters. Prentice Hall, Englewood Cliffs.

Durov, S.A., 1948. Natural waters and graphic representation of their composition. Dokl. Akad. Nauk SSSR 59, 87–90.

Edmunds, W.M., 2001. Palaeowaters in European coastal aquifers—the goals and main conclusions of the PALAEAUX project. Geol.Soc.Lond.Spec.Publ. 189 (1), 1–16.

El Halimi, N., Chaouni Alia, A., Beeuwsaert, E., Walraevens, K., 2001. Hydrogeological and geophysical investigation for characterizing the groundwater reservoir in Saidia Plain (north-eastern Morocco). In: Walraevens, K. (Ed.), Development of Water Resource Management Tools for Problems of Seawater Intrusion and Contamination of Fresh-Water Resources in Coastal Aquifers. Ghent University, Ghent.

Fadili, A., Mehdi, K., Riss, J., Najib, S., Makan, A., Boutayab, K., 2015. Evaluation of groundwater mineralization processes and seawater intrusion extension in the coastal aquifer of Oualidia, Morocco: hydrochemical and geophysical approach. Arab. J. Geosci. 8, 8567–8582.

Fehdi, C., Rouabhia, A., Baali, F., Boudoukha, A., 2009. The hydrogeochemical characterization of Morsott-El Aouinet aquifer, Northeastern Algeria. Environ. Geol. 58, 1611–1620. https://doi.org/10.1007/s00254-008-1667-4.

Felisa, G., Ciriello, V., Di Federico, V., 2013. Saltwater intrusion in coastal aquifers: a primary case study along the adriatic coast investigated within a probabilistic framework. Water 5, 1830–1847. https://doi.org/10.3390/w5041830.

Fidelibus, M.D., 2003. Environmental tracing in coastal aquifers: old problems and new solutions. In: Lopez-Geta, J.A., de Dios Gomez, J., de la Orden, J.A., Ramos, G., Rodriguez, L. (Eds.), Coastal Aquifers Intrusion Technology: Mediterranean Countries. IGME, Madrid, pp. 79–111.

Figoli, A., Fuoco, I., Apollaro, C., Chabane, M., Mancuso, R., Gabriele, B., De Rosa, R., Vespasiano, G., Barca, D., Criscuoli, A., 2020. Arsenic-contaminated groundwaters remediation by nanofiltration. Sep. Purif. Technol. 238, 116461.

Flury, M., Prapitz, A., 1993. Bromide in the natural environment: occurrence and toxicity. J. Environ. Qual. 22, 747–758.

Food and Agriculture Organization (FAO),). Land & Water https://www.fao.org/land-water/databases-and-software/crop-information/olive/en/ (accessed on 2 October 2021).

Franceschini, F., Signorini, R., 2016. Seawater intrusion via surface water vs. deep shoreline salt-wedge: a case history from the Pisa coastal plain (Italy). Groundw. Sustain. Dev. 2, 73–84.

Fuoco, I., Marini, L., De Rosa, R., Figoli, A., Gabriele, B., Apollaro, C., 2022. Use of reaction path modelling to investigate the evolution of water chemistry in shallow to deep crystalline aquifers with a special focus on fluoride. Sci. Total Environ. 830, 154566.
Galli, P., Bosi, V., 2002. Paleoseismology along the Cittanova fault: implications for seismotectonics and earthquake recurrence in Calabria (southern Italy). J. Geophys. Res. 107, 2044. https://doi.org/10.1029/2001JB000234.
Galli, P., Peronace, E., 2015. E. Low slip rates and multimillennial return times for Mw 7 earthquake faults in southern Calabria (Italy). Geophys. Res. Lett. 42, 5258–5265. https://doi.org/10.1002/2015GL064062.
Ganyaglo, S.Y., Osae, S., Akiti, T., Armah, T., Vitvar, T., Ito, M., Otoo, I.A., 2017. Application of geochemical and stable isotopic tracers to investigate groundwater salinity in the Ochi-Narkwa Basin Ghana. Hydrol. Sci. J. 62 (8), 1301–1316.
Garrels, R.M., 1968. Genesis of some ground waters from igneous rocks. In: Abelson, P.H. (Ed.)Researches in Geochemistryvol. 2. Wiley, New York, pp. 406–420.
Gat, J.R., 1996. Oxygen and hydrogen isotopes in the hydrologic cycle. Annu. Rev. Earth Planet. Sci. 24, 225–262.
Giambastiani, B.M.S., Kidanemariam, A., Dagnew, A., Antonellini, M., 2021. Evolution of salinity and water table level of the phreatic coastal aquifer of the Emilia Romagna Region (Italy). Water 13, 372. https://doi.org/10.3390/w13030372.
Giménez-Forcada, E., Sánchez San Román, F.J., 2015. An Excel macro to plot the HFE-diagram to identify sea water intrusion phases. Groundwater 53 (5), 819–824.
Giménez-Forcada, E., Bencini, A., Pranzini, G., 2010. Hydrogeochemical considerations about the origin of groundwater salinization in some coastal plains of Elba Island (Tuscany, Italy). Environ. Geochem. Health 32, 243–257.
Giustini, F., Brilli, M., Patera, A., 2016. Mapping oxygen stable isotopes of precipitation in Italy. J.Hydrol.Reg.Stud. 8, 162–181.
Grassi, S., Cortecci, G., Squarci, P., 2007. Groundwater resource degradation in coastal plains: the example of the Cecina area (Tuscany–Central Italy). Appl. Geochem. 22 (11), 2273–2289.
Han, D., Currell, M.J., Guo, H., 2021. Controls on distributions of sulphate, fluoride, and salinity in aquitard porewater from the North China Plain: long-term implications for groundwater quality. J. Hydrol. 603, 126828.
Helgeson, H.C., 1968. Evaluation of irreversible reactions in geochemical processes involving minerals and aqueous solutions—I.Thermodynamic relations. Geochim. Cosmochim. Acta 32 (8), 853–877.
Holzapfel, E., Merino, R., Mariño, M., Matta, R., 2000. Water production functions in kiwi. Irrig. Sci. 19, 73–79.
ISPRA, 2016. Foglio 590-Taurianova. Carta Geologica d'Italia alla Scala 1:50.000. Istituto Superiore per la Protezione e la Ricerca Ambientale, Roma.
Iyalomhe, F., Rizzi, J., Pasini, S., Torresan, S., Critto, A., Marcomini, A., 2015. Regional risk assessment for climate change impacts on coastal aquifers. Sci. Total Environ. 537, 100–114. https://doi.org/10.1016/j.scitotenv.2015.06.111.
Jacques, E., Monaco, C., Tapponnier, P., Tortorici, L., Winter, T., 2001. Faulting and earthquake triggering during the 1783 Calabria seismic sequence. Geophys. J. Int. 147, 499–516.
Kammoun, S., Trabelsi, R., Re, V., Zouari, K., 2021. Coastal aquifer salinization in semi-arid regions: the case of Grombalia (Tunisia). Water 13 (2), 129.
Kennedy, V.C., Zellweger, G.W., Jones, B.F., 1974. Filter pore-size effects on the analysis of Al, Fe, Mn, and Ti in water. Water Resour. Res. 10 (4), 785–790.
Khairy, H., Janardhana, M., 2013. Hydrogeochemical features of groundwater of semiconfined coastal aquifer in Amol-Ghaemshahr plain, Mazandaran Province, Northern Iran. Environ. Monit. Assess. 185, 9237–9264.
Kushnir, J., 1980. The coprecipitation of strontium, magnesium, sodium, potassium and chloride ions with gypsum.An experimental study. Geochim. Cosmochim. Acta 44 (10), 1471–1482.
Langman, J.B., Ellis, A.S., 2010. Multi-isotope (δD, δ18O, 87Sr/86Sr, and δ11B) approach for identifying saltwater intrusion and resolving groundwater evolution along the Western Caprock Escarpment of theSouthern High Plains, New Mexico. Appl.Geochem. 2 25, 159–174.
Laxen, D.P., Chandler, I.M., 1982. Comparison of filtration techniques for size distribution in freshwaters. Anal. Chem. 54 (8), 1350–1355.
Li, C., Gao, X., Liu, Y., Wang, Y., 2019. Impact of anthropogenic activities on the enrichment of fluoride and salinity in groundwater in the Yuncheng Basin constrained by Cl/Br ratio, δ18O, δ2H, δ13C and δ7Li isotopes. J. Hydrol. 579, 124211.
Longhitano, S.G., Chiarella, D., Di Stefano, A., Messina, C., Sabato, L., Tropeano, M., 2012. Tidal signatures in Neogene to Quaternary mixed deposits of southern Italy straits and bays. Sediment. Geol. 279, 74–96. https://doi.org/10.1016/j.sedgeo.2011.04.019.
Longinelli, A., Selmo, E., 2003. Isotopic composition of precipitation in Italy: a first overall map. J. Hydrol. 270 (1–2), 75–88.
Loreto, M.F., Düşünür-Doğan, D., Üner, S., İşcan-Alp, Y., Ocakoğlu, N., Cocchi, L., Muccini, F., Giordano, P., Ligi, M., 2019. Fault-controlled deep hydrothermal flow in a back-arc tectonic setting,SE Tyrrhenian Sea. Sci. Rep. 9 (1), 1–14.
Mallick, J., Singh, C.K., AlMesfer, M.K., Kumar, A., Khan, R.A., Islam, S., Rahman, A., 2018. Hydro-geochemical assessment of groundwater quality in Aseer Region, Saudi Arabia. Water 10, 1–14. https://doi.org/10.3390/w10121847.
Marconi, V., Antonellini, M., Balugani, E., Dinelli, E., 2011. Hydrogeochemical characterization of small coastal wetlands and forests in the Southern Po plain (Northern Italy). Ecohydrology 4, 597–607.
Marini, L., 2006. Geological Sequestration of Carbon Dioxide - Thermodynamics, Kinetics, and Reaction Path Modeling. Elsevier Science, Amsterdam.
Marini, L., Bonaria, V., Guidi, M., Hunziker, J.C., Ottonello, G., Zuccolini, M.V., 2000. Fluid geochemistry of the Acqui Terme-Visone geothermal area (Piemonte, Italy). Appl. Geochem. 15 (7), 917–935.
Martínez, M.L., Intralawan, A., Vázquez, G., Pérez-Maqueo, O., Sutton, P., Landgrave, R., 2007. The coasts of our world: ecological, economic and social importance. Ecol. Econ. 63 (2–3), 254–272.
Masciopinto, C., 2006. Simulation of coastal groundwater remediation: the case of Nardò fractured aquifer in Southern Italy. Environ. Model. Softw. 21, 85–97.
Mastrocicco, M., Colombani, N., 2020. The issue of groundwater salinization in coastal areas of the Mediterranean region: a review. Water 13, 90. https://doi.org/10.3390/w13010090.
Mastrocicco, M., Gervasio, M.P., Busico, G., Colombani, N., 2021. Natural and anthropogenic factors driving groundwater resources salinization for agriculture use in the Campania plains (Southern Italy). Sci. Total Environ. 758, 144033.
Matiatos, I., Paraskevopoulou, V., Lazogiannis, K., Botsou, F., Dassenakis, M., Ghionis, G., Alexopoulos, J.D., Poulos, S.E., 2018. Surface–ground water interactions and hydrogeochemical evolution in a fluvio-deltaic setting: the case study of the Pinios River delta. J. Hydrol. 561, 236–249.
McGranahan, G., Balk, D., Anderson, B., 2007. The rising tide: assessing the risks of climate change and human settlements in low elevation coastal zones. Environ. Urban. 19 (1), 17–37.
Menció, A., Mas-Pla, J., Otero, N., Regàs, O., Boy-Roura, M., Puig, R., Bach, J., Domènech, C., Zamorano, M., Brusi, D., Folch, A., 2016. Nitrate pollution of groundwater; all right…, but nothing else? Sci. Total Environ. 539, 241–251.
Mendizabal, I., Baggelaar, P.C., Stuyfzand, P.J., 2012. Hydrochemical trends for public supply well fields in the Netherlands (1898–2008), natural backgrounds and upscaling to groundwater bodies. J. Hydrol. 450 (451), 279–292.
Menichini, M., Doveri, M., 2020. Modelling tools for quantitative evaluations on the Versilia coastal aquifer system (Tuscany, Italy) in terms of groundwater components and possible effects of climate extreme events.Acque Sotterranee. Ital. J. Groundw. 9 (3), 35–44. https://doi.org/10.7343/as-2020-475.
Mjemah, I.C., Van Camp, M., Walraevens, K., 2009. Groundwater exploitation and hydraulic parameter estimation for a quaternary aquifer in Dar-Es-Salaam,Tanzania. J. Afr. Earth Sci. 55, 134–146.
Mollema, P.N., Antonellini, M., Dinelli, E., Gabbianelli, G., Greggio, N., Stuyfzand, P.J., 2013. Hydrochemical and physical processes influencing salinization and freshening in Mediterranean low-lying coastal environments. Appl. Geochem. 34, 207–221.
Monaco, C., Tortorici, L., 2000. Active faulting in the Calabrian arc and eastern Sicily. J. Geodyn. 29, 407–424.
Mtoni, Y., Chikira, I.C.M., Bakundukize, C., Van Camp, M., Martens, K., Walraevens, K., 2013. Saltwater intrusion and nitrate pollution in the coastal aquifer of Dar es Salaam Tanzania. Environ. Earth Sci. 70, 1091–1111. https://doi.org/10.1007/s12665-012-2197-7.
Muraoka, H., Takahashi, M., Sundhoro, H., Dwipa, S., Soeda, Y., Momit, M., Shimada, K., 2010. Geothermal systems constrained by the Sumatran Fault and its pull-apart basins in Sumatra, Western Indonesia. Proceedings World Geothermal Congress, Bali, Indonesia, pp. 25–29.
Muzzillo, R., Zuffianò, L.E., Rizzo, E., Canora, F., Capozzoli, L., Giampaolo, V., De Giorgio, G., Sdao, F., Polemio, M., 2021. Seawater intrusion proneness and geophysical investigations in the Metaponto coastal plain (Basilicata, Italy). Water 13 (1), 53. https://doi.org/10.3390/w13010053.
Nasher, G., Al-Sayyaghi, A., Al-Matary, A., 2013. Identification and evaluation of the hydrogeochemical processes of the lower part of Wadi Siham catchment area, Tihama plain, Yemen. Arab. J. Geosci. 6, 2131–2146.
Nisi, B., Vaselli, O., Huertas, A.D., Tassi, F., 2013. Dissolved nitrates in the groundwater of the Cecina Plain (Tuscany, Central-Western Italy): clues from the isotopic signature of NO3. Appl. Geochem. 34, 38–52.
Nisi, B., Vaselli, O., Elio, J., Giannini, L., Tassi, F., Guidi, M., Darrah, T.H., Maletic, E.L., Delgado Huertas, A., Marchionni, S., 2019. The Campo de Calatrava Volcanic Field (central Spain): fluid geochemistry in a CO2-rich area. Appl.Geochem. 102, 153–170. https://doi.org/10.1016/j.apgeochem.2019.01.011.
Nisi, B., Vaselli, O., Taussi, M., Doveri, M., Menichini, M., Cabassi, J., Raco, B., Botteghi, S., Mussi, M., Masetti, G., 2022. Hydrogeochemical surveys of shallow coastal aquifers: a conceptual model to set-up a monitoring network and increase the resilience of a strategic groundwater system to climate change and anthropogenic pressure. Appl. Geochem. 142. https://doi.org/10.1016/j.apgeochem.2022.105350.
Nollet, L.M.L., De Gelder, L.S.P., 2007. Handbook of Water Analysis. second ed. Taylor & Francis, London https://doi.org/10.1201/9781420006315.
Nordstrom, D.K., 1997. Thermochemical redox equilibria of ZoBell's solution. Geochim. Cosmochim. Acta 41, 1835–1841.
Palandri, J.L., Reed, M.H., 2001. Reconstruction of in situ composition of sedimentary formation waters. Geochim. Cosmochim. Acta 65, 1741–1767.
Parkhurst, D.L., Appelo, C.A.J., 1999. User's guide to PHREEQC (Version 2): a computer program for speciation, batch-reaction, one-dimensional transport, and inverse geochemical calculations. Water-resources Investigations Report. U.S. Geological Survey, pp. 99–4259.
Pastorelli, S., Marini, L., Hunziker, J.C., 2001. Chemistry, isotope values (δD, δ18O, δ34SSO4) and temperatures of the water inflows in two Gotthard tunnels, Swiss Alps. Appl. Geochem. 16, 633–649.
Petalas, C., Pisinaras, V., Gemitzi, A., Tsihrintzis, V.A., Ouzounis, K., 2009. Current conditions of saltwater intrusion in the coastal rhodope aquifer system, northeastern Greece. Desalination 237 (1–3), 22–41.
Pfahl, S., Sodemann, H., 2014. What controls deuterium excess in global precipitation? Clim. Past 10 (2), 771–781.
Phocaides, A., 2000. Handbook on Pressurized Irrigation Techniques. FAO, Roma.
Pierre, C., 1999. The oxygen and carbon isotope distribution in the Mediterranean water masses. Mar. Geol. 153 (1–4), 41–55.
Pizzino, L., Burrato, P., Quattrocchi, F., Valensise, G., 2004. Geochemical signatures of large active faults: the example of the 5 February 1783, Calabrian earthquake (southern Italy). J. Seismol. 8, 363–380.
Polemio, M., Walraevens, K., 2019. Recent research results on groundwater resources and saltwater intrusion in a changing environment. Water 11 (6), 1118. https://doi.org/10.3390/w11061118.

Polemio, M., Zuffianò, L.E., 2020. Review of utilization management of groundwater at risk of salinization. J. Water Resour. Plan. Manag. 146 (9), 03120002.
Randazzo, P., Caracausi, A., Aiuppa, A., Cardellini, C., Chiodini, G., Apollaro, C., Paternoster, M., Rosiello, A., Vespasiano, G., 2022. Active degassing of crustal CO2 in areas of tectonic collision: a case study from the Pollino and Calabria sectors (Southern Italy). Front. Earth Sci. 10, 946707. https://doi.org/10.3389/feart.2022.946707.
Reimann, C., De Caritat, P., 1998. Chemical Elements in the Environment. Springer, New York, Inc., New York 397 p.
Rickard, D., 2012. Sulfidic Sediments and Sedimentary Rocks. Elsevier, Amsterdam.
Rickard, D., Mussmann, M., Steadman, J.A., 2017. Sedimentary sulfides. Elements 13 (2), 117–122.
Sarker, M.M.R., Van Camp, M., Hossain, D., Islam, M., Ahmed, N., Karim, M.M., Bhuiyan, Md. A.Q., Walraevens, K., 2021. Groundwater salinization and freshening processes in coastal aquifers from southwest Bangladesh. Sci. Total Environ. 779, 146339.
Schmidt, G.A., 1999. Forward modeling of carbonate proxy data from planktonic foraminifera using oxygen isotope tracers in a global ocean model. Paleoceanography 14 (4), 482–497.
Seal, R.R., 2006. Sulfur isotope geochemistry of sulfide minerals. Rev. Mineral. Geochem. 61 (1), 633–677.
Stenni, B., Nichetto, P., Bregant, D., Scarazzato, P., Longinelli, A., 1995. The Delta-O-18 signal of the northward flow of mediterranean waters in the adriatic sea. Oceanol. Acta 18 (3), 319–328.
Stewart, F.H., 1963. Marine evaporites. Data of Geochemistry, 6th ed.U.S. Geological Survey Professional Paper 440-Y 52 p.
Steyl, G., Dennis, I., 2010. Review of coastal-area aquifers in Africa. Hydrogeol. J. 18, 217–225.
Stumm, W., Morgan, J.J., 1996. Aquatic Chemistry: Chemical Equilibria and Rates in Natural Waters. third ed. Wiley, New York.
Stuyfzand, P., 1986. A New Hydrochemical Classification of Water Types With Examples of Application to the Netherlands. H20 19, pp. 562–568.
Stuyfzand, P.J., 1989. A New Hydrochemical Classification of Water Types. 182. IAHS Publ., pp. 89–98.
Stuyfzand, P.J., 2008. Base exchange indices as indicators of salinization or freshening of (coastal) aquifers. 20th Salt Water Intrusion Meeting, Naples, Florida, USA. IFAS Research, Gainesville.
Sudaryanto, Naily, W., 2018. Ratio of major ions in groundwater to determine saltwater intrusion in coastal areas. Conf. Ser.: Environ. Earth Sci 118, 012021.
Tassi, F., Capecchiacci, F., Giannini, L., Vougiokalakis, G., Vaselli, O., 2013. Volatile organic compounds (VOCs) in air from Nisyros Island (Dodecanese Archipelago, Greece): natural versus anthropogenic sources. Environ. Pollut., 180 https://doi.org/10.1016/j.envpol.2013.05.023.
Taussi, M., Gozzi, C., Vaselli, O., Cabassi, J., Menichini, M., Doveri, M., Romei, M., Ferretti, A., Gambioli, A., Nisi, B., 2022. Contamination assessment and temporal evolution of nitrates in the shallow aquifer of the Metauro River Plain (Adriatic Sea, Italy) after remediation actions. Int. J. Environ. Res. PublicHealth 19 (19), 12231. https://doi.org/10.3390/ijerph191912231.
Torres-Martínez, J.A., Mora, A., Mahlknecht, J., Daesslé, L.W., Cervantes-Avilés, P.A., Ledesma-Ruiz, R., 2021. Estimation of nitrate pollution sources and transformations in groundwater of an intensive livestock-agricultural area (Comarca Lagunera), combining major ions, stable isotopes and MixSIAR model. Environ. Pollut. 269, 115445.
Tripodi, V., Muto, F., Brutto, F., Perri, F., Critelli, S., 2018. NeogenQuaternary evolution of the forearc and backarc regions between the Serre and Aspromonte Massifs, Calabria (southern Italy). Mar. Pet. Geol. 95, 328–343.
Turekian, K.K., Wedepohl, K.H., 1961. Distribution of the elements in some major units of the earth's crust. Geol. Soc. Am. Bull. 72 (2), 175–192.
Van Camp, M., Mjemah, I.C., Alfarrah, N., Walraevens, K., 2013. Modeling approaches and strategies for data-scarce aquifers: example of the Dar es Salaam aquifer in Tanzania. Hydrogeol. J. 21, 341–356.
Van Camp, M., Mtoni, Y.E., Mjemah, I.C., Bakundukize, C., Walraevens, K., 2014. Investigating seawater intrusion due to groundwater pumping with schematic model simulations: the example of the Dar es Salaam coastal aquifer in Tanzania. J. Afr. Earth Sci. 96, 71–78.
Vandenbohede, A., Lebbe, L., 2012. Groundwater chemistry patterns in the phreatic aquifer of the central Belgian coastal plain. Appl.Geochem. 27, 22–36.
Vardè, M., Servidio, A., Vespasiano, G., Pasti, L., Cavazzini, A., Di Traglia, M., Rosselli, A., Cofone, F., Apollaro, C., Cairns, W.R., Scalabrin, E., 2019. Ultra-trace determination of total mercury in Italian bottled waters. Chemosphere 219, 896–913.
Vaselli, O., Lazzaroni, M., Nisi, B., Cabassi, J., Tassi, F., Rappuoli, D., Meloni, F., 2021. Discontinuous geochemical monitoring of the Galleria Italia circumneutral waters (former Hg-mining area of Abbadia San Salvatore, Tuscany, Central Italy) feeding the Fosso Della Chiusa Creek. Environment 8, 15. https://doi.org/10.3390/environments8020015.
Vespasiano, G., Apollaro, C., Muto, F., Dotsika, E., De Rosa, R., Marini, L., 2014. Chemical and isotopic characteristics of the warm and cold waters of the Luigiane Spa near Guardia Piemontese (Calabria, Italy) in a complex faulted geological framework. Appl. Geochem. 41, 73–88.
Vespasiano, G., Apollaro, C., Marini, L., Dominici, R., Cianflone, G., Romanazzi, A., Polemio, M., De Rosa, R., 2015a. Hydrogeological and isotopic study of the multi-aquifer system of the Sibari Plain (Calabria, Southern Italy). Rend. Online Soc. Geol. It. 39, 134–137.
Vespasiano, G., Apollaro, C., De Rosa, R., Muto, F., Larosa, S., Fiebig, J., Mulch, A., Marini, L., 2015b. The small spring method (SSM) for the definition of stable isotope - elevation relationships in Northern Calabria (Southern Italy). Appl. Geochem. 63, 333–346.
Vespasiano, G., Cianflone, G., Cannata, C.B., Apollaro, C., Dominici, R., De Rosa, R., 2016. Analysis of groundwater pollution in the Sant'Eufemia Plain (Calabria – South Italy). Ital.J.Eng.Geol.Environ. 2, 5–15. https://doi.org/10.4408/IJEGE.2016-02.O-01.
Vespasiano, G., Cianflone, G., Romanazzi, A., Apollaro, C., Dominici, R., Polemio, M., De Rosa, R., 2019. A multidisciplinary approach for sustainable management of a complex coastal plain: the case of Sibari Plain (Southern Italy). Mar. Pet. Geol. 109, 740–759. https://doi.org/10.1016/j.marpetgeo.2019.06.031.
Vespasiano, G., Marini, L., Muto, F., Auqué, L.F., Cipriani, M., De Rosa, R., Critelli, S., Gimeno, M.J., Blasco, M., Dotsika, E., Apollaro, C., 2021a. Chemical, isotopic and geotectonic relations of the warm and cold waters of the Cotronei (Ponte Coniglio), Bruciarello and Repole thermal areas, (Calabria - southern Italy). Geothermics 96. https://doi.org/10.1016/j.geothermics.2021.102228.
Vespasiano, G., Muto, F., Apollaro, C., 2021b. Geochemical, geological and groundwater quality characterization of a complex geological framework: the case study of the Coreca area (Calabria, South Italy). Geosciences 11 (3), 121. https://doi.org/10.3390/geosciences11030121.
Walraevens, K., Mjemah, I.C., Mtoni, Y., Van Camp, M., 2015. Sources of salinity and urban pollution in the quaternary sand aquifers of Dar Es Salaam,Tanzania. J. Afr. Earth Sci. 102, 149–165.
Werner, A.D., 2010. A review of seawater intrusion and its management in Australia. Hydrogeol. J. 18, 281–285.
White, A.F., Bullen, T.D., Vivit, D.V., Schulz, M.S., Clow, D.W., 1999. The role of disseminated calcite in the chemical weathering of granitoid rocks. Geochim. Cosmochim. Acta 63 (13–14), 1939–1953.
White, A.F., Schulz, M.S., Lowenstern, J.B., Vivit, D.V., Bullen, T.D., 2005. The ubiquitous nature of accessory calcite in granitoid rocks: implications for weathering, solute evolution, and petrogenesis. Geochim. Cosmochim. Acta 69, 1455–1471.
Wua, X., Zhangb, L., Hub, B.X., Yang Wangb, Y., Xue, Z., 2020. Isotopic and hydrochemical evidence for the salinity origin in the coastal aquifers of the Pearl River Delta, Guangzhou,China. J. Contam. Hydrol. 235, 103732. https://doi.org/10.1016/j.jconhyd.2020.103732.
Zarei, M., Raeisi, E., Merkel, B.J., 2012. Identifying sources of salinization using hydrochemical and isotopic techniques Konarsiah,Iran. Environ. Earth Sci. 70 (2), 1. https://doi.org/10.1007/s12665-012-2143-8.